Constitutive Characterization of a Rare-earth Magnesium Alloy Sheet (ZEK100-O) in Shear Loading: Studies of Anisotropy and Rate Sensitivity

A. Abedini*, C. Butcher, M.J. Nemcko, S. Kurukuri, M.J. Worswick

*Corresponding author. Email Address: aabedini@uwaterloo.ca

Department of Mechanical and Mechatronics Engineering, University of Waterloo, Waterloo, ON, CANADA

Abstract: Rare-earth magnesium alloys such as ZEK100-O offer improved ductility over other conventional magnesium alloys at room temperature; however, they exhibit significant anisotropy and complex yield behaviour. In this work, a systematic investigation of anisotropy of ZEK100-O rolled sheet in shear loading was conducted at room temperature under quasi-static conditions, as the shear deformation of these alloys is not well understood. Furthermore, uniaxial tensile and compressive characterization of the material was performed to provide context for its behaviour under shear loading. It was revealed that ZEK100-O exhibits strong anisotropy in shear which is markedly different than tensile anisotropy with unique trends that suggest the activation of different deformation mechanisms. To characterize shear anisotropy in HCP materials such as ZEK100-O, the shear response of the material should be investigated in three orientations of 0° (or 90°), 45°, and 135° with respect to the rolling direction. The selection and analysis of these directions is discussed in terms of the principal stress directions and activation of different deformations mechanisms. In order to further investigate this behaviour, the microstructure of the deformed specimens was studied using Electron Backscattered Diffraction (EBSD) analysis to quantify the active twinning systems in different test orientations. Moreover, the CPB06 yield criterion with two linear transformations was calibrated with experimental data to describe the complex anisotropic behaviour of ZEK100-O. It was established that the material exhibits asymmetry not only in tension-compression regions represented by the 1^{st} and 3^{rd} quadrants of yield locus but also in shear regions represented by the 2^{nd} and 4^{th} quadrants. Finally, the strain rate sensitivity of ZEK100-O was studied in shear tests at elevated strain rates of 10 s^{-1} and 100 s^{-1}, at which positive rate sensitivity was observed.

Keywords: Anisotropic material; Shear loading; Rare-earth magnesium alloy

1. Introduction

In recent years, there has been an increasing demand to reduce the weight of vehicles to tackle the global issues of energy conservation and environmental protection. Lightweighting of vehicles can be accomplished using a variety of methods with the main approaches involving a shift from traditional steel alloys towards the adoption of low density alloys such as aluminum and magnesium. Specifically, rare-earth magnesium alloys have the potential to be used as light-weight structural alloys since they possess a weakened crystallographic texture that leads to superior ductility over conventional magnesium alloys. However, a strong orientation dependency persists in these materials leading to a strong anisotropic response. As a result, these alloys need extensive material characterization to develop and calibrate advanced constitutive models and fracture criteria where the shear state provides a fundamental loading mode that is critical for the calibration of anisotropic yield criteria and fracture models.

Often, the shear response of ductile materials is determined by conducting torsion tests on thin walled tubular samples (Montheillet *et al*., 1984; Stout and O'Rourke, 1989; Peirs *et al*., 2011a; Yoshida *et al*., 2014); however, this test method is not suitable for sheet materials without substantial modifications of testing apparatus and procedure, such as was done by Tekkaya and Pöhlandt (1982) and Yin *et al.* (2011, 2012) who performed in-plane torsion tests. Iosipescu (1967) designed one of the first methods for the shear testing of sheet materials by using notched specimens subjected to four-point bending. More recent studies utilize a rectangular-shaped specimen that is mechanically clamped on opposite sides with a shear deformation applied by moving the clamps parallel to each other in opposite directions. This method of shear testing and its extensions have been used to study the shear response of a large number of sheet metals (Gasperini *et al.,* 1996; Bae and Ghosh, 2003; Bouvier *et al.,* 2006; Mohr and Henn, 2007; Lou *et al*., 2007; Rauch, 2009; Carbonniere *et al*., 2009; Thuillier and Manach, 2009; Dunand and Mohr, 2011; Abedini *et al.,* 2015; Abedini *et al.,* 2017). Alternatively, a number of studies have involved designing complex shear test geometries with the aid of Finite Element (FE) simulations in which a tensile load is converted to a shear stress in the gauge area of the samples (Bao and Wierzbicki, 2004; Tarigopula *et al*., 2008; Brunig *et al*., 2008; Kang *et al*., 2008; Lademo *et al*., 2009; Reyes *et al*., 2009; Gao *et al*., 2011; Gruben *et al*., 2011; Lian *et al*., 2012; Peirs *et al*., 2011b, 2012). Recently, a novel shear sample geometry of this type was introduced

by Peirs *et al*. (2012) for both quasi-static and dynamic loading conditions. The advantage of this test geometry is that it has a relatively simple design and does not require through-thickness machining that may introduce surface defects.

Shear characterization of materials at elevated rates of strain is also important for accurate modelling of sheet metal forming and vehicle crash simulations. Shear testing under dynamic strain rates were initially conducted by Campbell and Fergusen (1970) by means of a double-notched specimen. Double-notched specimens were further modified in the literature to obtain a more homogeneous shear strain in the gauge area of the specimen (Klepaczko, 1994; Klepaczko *et al*., 1999; Rusinek and Klepaczko, 2001; Bonnet-Lebouvier *et al*., 2002; Hubnatter and Merklein, 2008; Guo and Li, 2012; Shi *et al*., 2014). Although double-notched specimens can be utilized for shear characterization of isotropic materials, it may complicate the interpretation of the response of anisotropic materials because the shear bands in each gauge section rotate in opposite directions, complicating the interpretation of the response and potentially averaging away the anisotropy of materials. Similar statements can be made for the so-called "smiley" specimens (Till and Hackl, 2013; Roth and Mohr, 2015) in which the rotation of the shear bands have similar characteristics to that of the double-notched specimen. Furthermore, machining defects and small misalignments in the test frame can cause deformation to localize and initiate in one of the two gauge regions.

The objective of the present work is to investigate the anisotropic response of a rare-earth magnesium alloy sheet (ZEK100-O) at low and elevated strain rates. The behaviour of a severely anisotropic HCP material in shear loading is not well understood and it may lead to complex material behaviour and evolving anisotropy through the activation of different deformation mechanisms including the twinning systems. A series of tensile, compressive, and shear characterization experiments were performed along with Electron Backscattered Diffraction (EBSD) analysis to determine the types of twins and relative fractions of the various twinning systems activated. A test methodology involving three shear tests is proposed to characterize shear anisotropy, and a strain-rate dependent constitutive relation and an anisotropic yield criterion were calibrated to the shear and uniaxial loading results.

2. Material

A commercial rare-earth magnesium alloy ZEK100 (O-temper) rolled sheet with a nominal thickness of 1.55 mm was used in the present study. The alloy was provided from Magnesium Elektron Inc. in an O-temper condition which indicates that the material has been annealed to remove cold work. The chemical composition of ZEK100-O is presented in Table 1. The undeformed material was mechanically ground and polished for microstructural observation. Table 2 outlines the material preparation procedure used for the X-Ray Diffraction (XRD) analysis. For the EBSD analysis, the initial sample preparation was identical to that described in Table 2, while the polished samples were also etched with argon using an ion milling machine. This procedure removes a fine layer (typically a few Ångströms in thickness) of material from the sample surface and is carried out here to remove surface oxidation. The inverse pole figure component map and pole figures of the undeformed texture are shown in Figure 1. It can be seen that the texture exhibits a spread of the basal poles along the transverse direction (TD) which is typical of rare-earth magnesium alloys (Kurukuri *et al.,* 2014a). In addition, the sample initially has a small fraction of twins within the microstructure.

Table 1 – Chemical composition of ZEK100-O.

	Zn	**Nd**	**Zr**	**Mn**	**Mg**
Chemical Composition (%wt)	1.3	0.2	0.25	0.01	balance

Table 2 – Material preparation procedure.

Surface	**Lubricant**	**Time (mins)**
2000 grit SiC paper	Water	1
4000 grit SiC paper	Water	2
3 µm diamond suspension	Struers DP Brown	5
1 µm diamond suspension	Struers DP Brown	5
0.05 µm colloidal silica suspension	80% Glycerol, 20% Reagent Alcohol	10

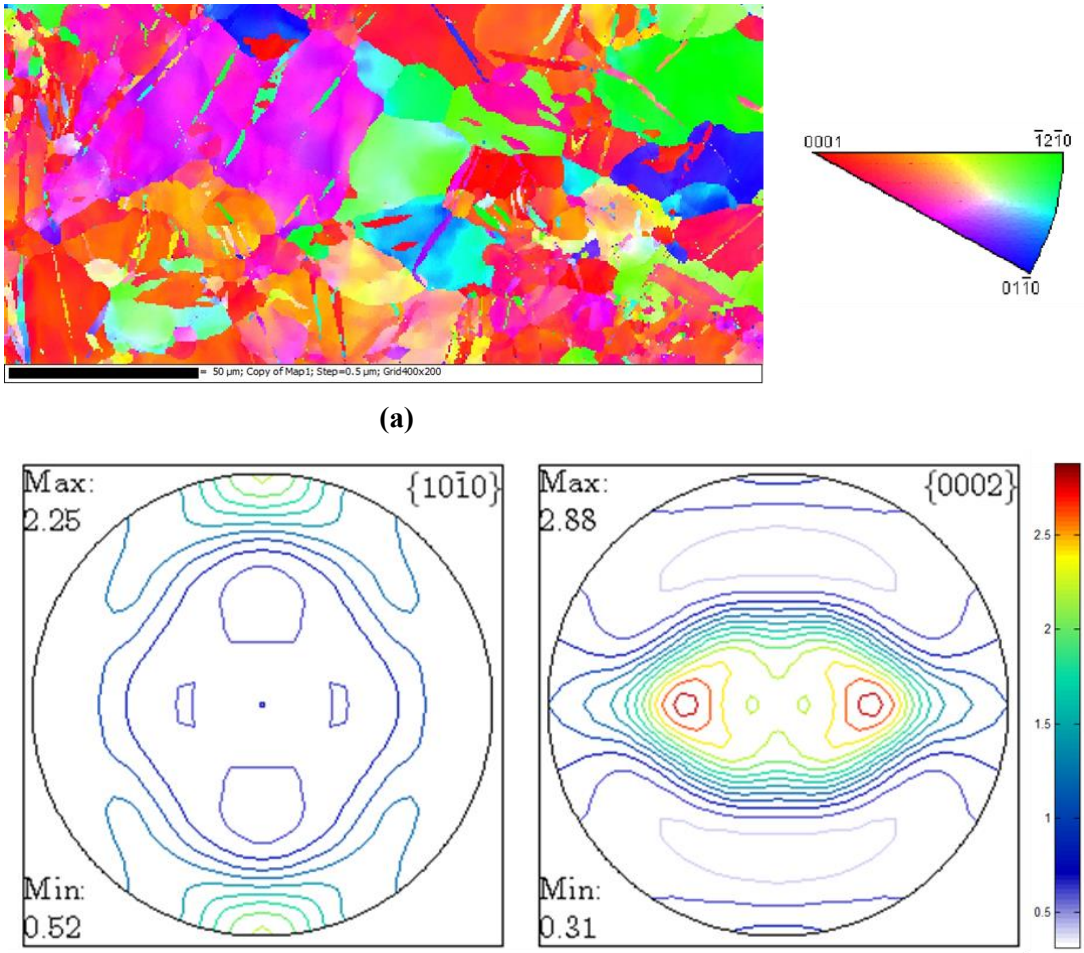

Figure 1 – (a) EBSD inverse pole figure component map, (b) $\{10\bar{1}0\}$, and (c) $\{0002\}$ XRD pole figures of the undeformed material.

3. Experiments and Methodology

The experimental procedure and method of extracting data are presented in this section. The methodologies for the tensile and compressive tests are given first for the baseline characterization followed by shear tests at quasi-static and elevated strain rates. Furthermore, the methods for strain measurements are introduced followed by a brief theoretical background on mechanics of shear deformation.

3.1. Uniaxial Tension Test

Uniaxial tensile tests were conducted using sub-sized ASTM E8 specimens under quasi-static conditions with samples extracted from the rolling (0° or RD), diagonal (45° or DD), and transverse (90° or TD) directions of the sheet. The geometry of the dogbone specimen is depicted in Figure 2. The tensile experiments were performed using an Instron model 1331 servo-hydraulic testing machine with a cross-head velocity of 0.025 mm/s to obtain a nominal strain rate of 0.001 s^{-1}. At least four tests per orientation were conducted to ensure the repeatability of the results.

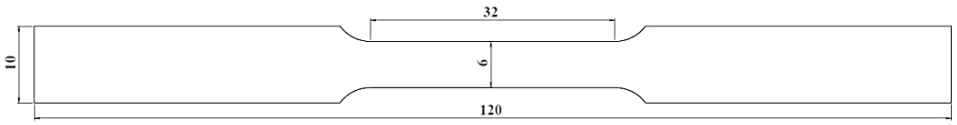

Figure 2 – Geometry of the uniaxial tensile specimen. All dimensions are in millimeters.

3.2. Uniaxial Compression Test

For uniaxial compression tests, the experimental methodology of Kurukuri *et al.* (2014a) and Steglich *et al.* (2014) was followed in which adhesively stacked samples were used to obtain the compressive response of sheet metals. Cubic specimens with aspect ratio of unity were fabricated in the three directions of RD, DD, and TD by adhesively bonding five layers of sheets, as depicted in Figure 3 and the specimens were tested using a compression device shown in Figure 3. To improve the performance of the adhesive, bonding surfaces of each sheet were roughened by light scoring, then the sheet layers were carefully cleaned using Acetone and J-B-Weld® adhesive was applied between the inner layers. After curing the adhesive for 24 hours, the surfaces of the specimen in contact with the upper and lower compression plates were polished to a mirror-finish. Furthermore, Teflon® spray was applied as lubricant to reduce friction between the specimens and the compression platens. The Instron machine was used to apply the compressive force to the specimens with a cross-head velocity of 0.008 mm/s to obtain a nominal strain rate of approximately 0.001 s^{-1}.

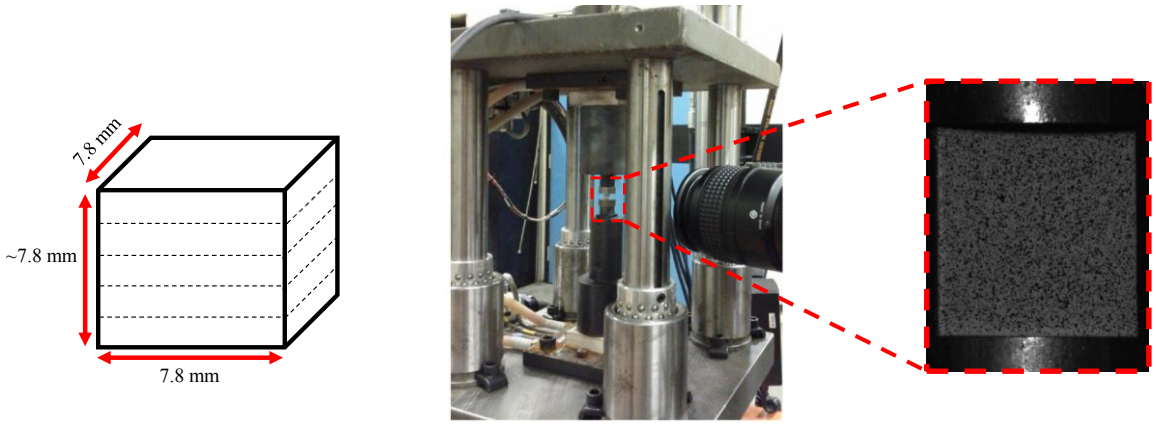

Figure 3 – Stacked compression specimen (left), compression testing device used to ensure alignment (center) and photograph of specimen showing speckle pattern for DIC-based strain measurement (right).

3.3. Shear Test under Quasi-static Condition

Peirs *et al*. (2012) developed the novel shear geometry shown in Figure 4 from a systematic FE study to design a simple shear test specimen. The design of this geometry is an evolution of the geometries proposed by Bao and Wierzbicki (2004) and Tarigopula *et al*. (2008). Due to the small size of the sample, it is referred to as the "mini-shear specimen" throughout this paper. The specimen geometry was designed so that the applied tensile load is converted to a shear stress in the gauge section of the specimen. The notches are offset by an eccentricity of 1 mm to provide a stress triaxiality very close to the theoretical value of zero for shear loading (Peirs *et al*., 2012).

This geometry has several advantages over its counterparts in the literature. In particular, its small geometry makes it suitable for testing under higher rates of strain and has a relatively simple geometry that is easy to fabricate. Contrary to a number of shear sample geometries in the literature (Kang *et al*., 2008; Bao and Wierzbicki, 2004; Brunig *et al*., 2008; Dunand and Mohr, 2011; Lian *et al*., 2012), it does not have a reduced thickness in the shear zone which avoids complications such as machining-induced surface defects and residual stresses that can initiate fracture. Shear samples were fabricated from ZEK100-O sheet to have the applied load in the 0°, 45°, 90°, and 135° directions with respect to the rolling direction. The mini-shear specimens were fabricated by CNC machining.

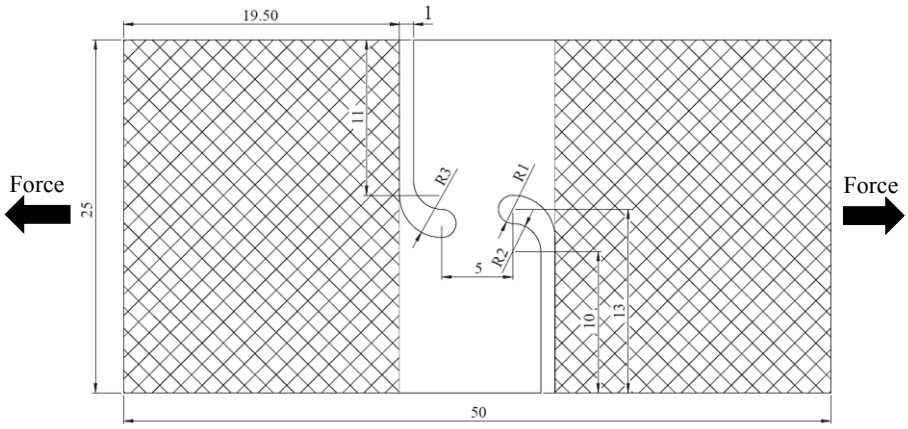

Figure 4 - Mini-shear specimen geometry of Peirs *et al.* (2012). All dimensions are in millimeters. The cross-hatched area is clamped in the grips of testing machines.

The average shear stress in the shear zone and the applied tensile force are directly related so that the average shear stress can be calculated by simply dividing the force by the shear area, as suggested by Peirs *et al*. (2012):

$$\tau = \frac{F}{A} = \frac{F}{L\,t} \tag{1}$$

where τ is the average shear stress, F is the force, t is the thickness, and L is the length of the shear region which is 3 mm. It was shown by Peirs *et al*. (2012) and Abedini *et al*. (2015) that the average shear stress calculated with Eq. (1) agrees very well with the finite element simulations results of local elements at the center of the gauge region. Also, it was shown experimentally by Abedini *et al*. (2015) that the through-thickness strains are negligible in this test leading to a constant shear area; therefore, the average shear stress obtained with Eq. (1) can be considered as both the engineering and true stress since the gauge region is small and the shear strain distribution is relatively uniform. The quasi-static tests for the mini-shear specimen were performed with the Instron testing machine with a cross-head velocity of 0.03 mm/s to obtain a von Mises equivalent true strain rate of 0.01 s^{-1}. Strain measurements were performed using *in situ* digital image correlation techniques as described in Section 3.5.

3.4. Shear Test under Elevated Strain Rates

The mini-shear specimen is also used in the present work to study the shear response of ZEK100-O at higher rates of strain. However, the width of the mini-shear specimen is larger than the grip slot sizes of the high speed hydraulic testing apparatus available at University of Waterloo. Thus, the mini-shear specimen was modified for high-rate applications by scaling down all the dimensions of the specimen by 36% (Figure 5). It was shown by Rahmaan *et al*. (2015) that the results of the reduced size mini-shear specimen are in excellent agreement with that of a full-size mini-shear sample for both an aluminium-magnesium alloy, AA5182-O, and a dual-phase steel, DP600. Therefore, in the present study, efforts to further validate the full-size *versus* scaled-down mini-shear specimens were not deemed necessary.

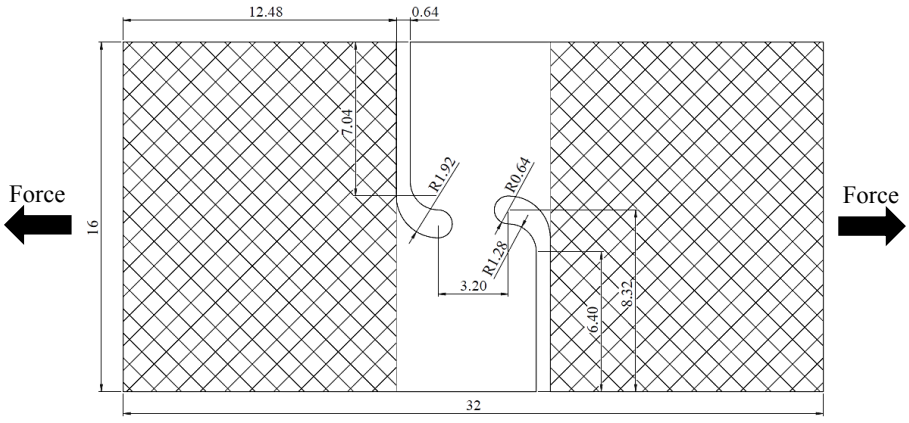

Figure 5 – Scaled-down mini-shear specimen from Rahmaan *et al.* (2015). All dimensions are in millimeters. The cross-hatched area is clamped in the grips of testing machines.

The shear tests with elevated strain rates were performed using a Hydraulic Intermediate Strain Rate (HISR) testing machine, described by Bardelcik *et al.* (2014), as shown in Figure 6. Cross-head velocities of 150 mm/s, and 900 mm/s were used to obtain average von Mises equivalent true strain rates of 10 s^{-1} and 100 s^{-1}, respectively. To assess the repeatability of the experimental results, for all the shear tests, at least four specimens per orientation were tested. The evolution of the equivalent strain rates with deformation are presented in Figure 7 for the test along the 45° direction. It was observed that the evolution of the strain rates in other

directions are similar to that of the 45° direction and the results for the other directions are not shown here for brevity.

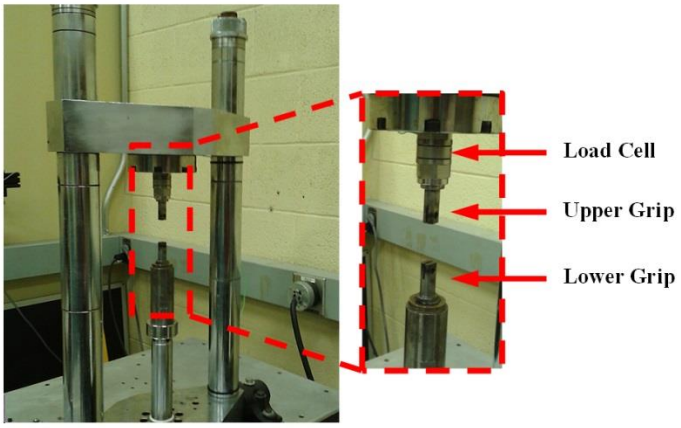

Figure 6 – Schematic of the HISR machine.

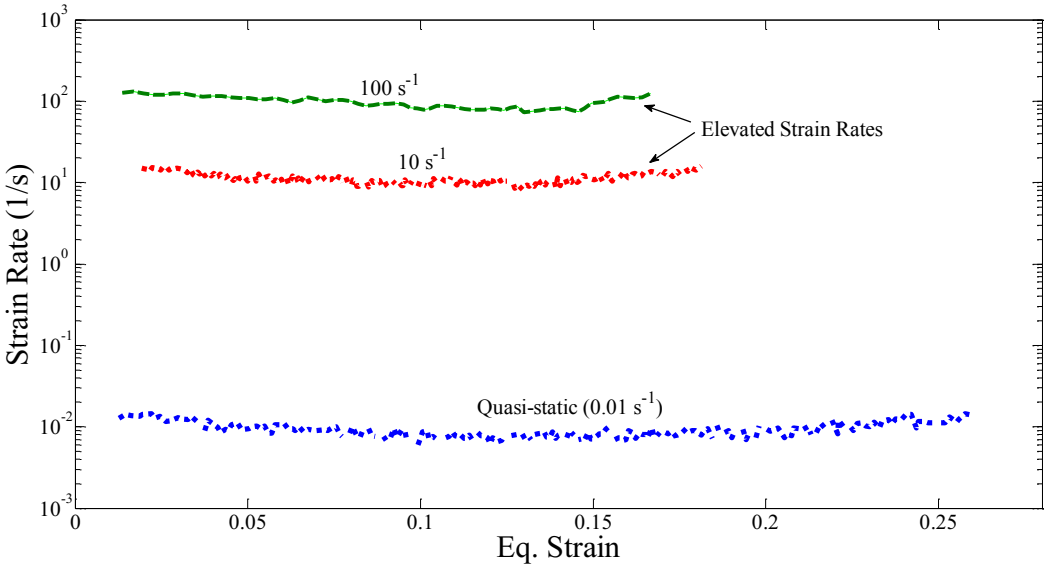

Figure 7 – Evolution of the von Mises equivalent true strain rate with the von Mises equivalent strain for ZEK100-O loaded in the 45° direction with respect to the rolling direction.

3.5. Strain Measurements

The experiments were recorded using digital cameras to obtain full-field logarithmic strain measurements using Digital Image Correlation (DIC) techniques. The commercial VIC2D and VIC3D DIC software packages from Correlated Solutions, Inc. were used to obtain the full-field strain measurements using the "incremental correlation" option to account for large local strains.

Tensile and Compressive Experiments: Stereo DIC was used for the uniaxial tests using Point Grey 5 MP cameras with 50 mm Nikon lenses at 2 frames per second. Full field strain measurements were obtained using an average subset size of 31 pixels, step size of 4 and a strain filter size of 9 pixels. Virtual extensometers were used to measure the strain of specimens in the longitudinal and width directions. The resolutions in the DIC area of interest were 0.021 mm/pixel and 0.011 mm/pixel for the uniaxial tensile and compressive tests, respectively.

Shear Experiments: All strain measurements for the mini-shear tests were obtained using 2-D digital image correlation techniques. Abedini *et al*. (2015, 2017) compared both stereo and 2-D DIC results of the mini-shear specimen and reported that using the simpler 2-D DIC is equivalent to stereo DIC to characterize the shear response due to the negligible through-thickness strains. For quasi-static loading of the mini-shear specimen, a Point Grey 4.1 MP camera with a 60 mm (1:2.8) Nikon lens was used to acquire images at a rate of 5 frames per second. The DIC settings used a subset size of 29 pixels, step size of 5 and strain filter of 9 pixels. The resolution in the DIC area of interest was 0.012 mm/pixel for the mini-shear tests.

For the elevated strain rate experiments, a high-speed Photron SA5 camera with a 105 mm (1:2.8) Sigma lens was used with frame rates of 18,600 and 40,000 frames per second for strain rates of 10 s^{-1} and 100 s^{-1}, respectively. A subset size of 25 pixels, step size of 4 and strain filter of 9 pixels were used for the tests with elevated strain rates. The resolution in the DIC area of interest was 0.016 mm/pixel for the scaled-down mini-shear tests.

The DIC strains were averaged using a circle with 0.5 mm diameter located at the center of the mini-shear specimen while for the scaled-down mini-shear specimen, the circle size was scaled accordingly (0.32 mm diameter). This method of extracting the DIC strains is appropriate for shear characterization of materials as explained in Rahmaan *et al.* (2015). It is important to state that the equivalent strain and strain rate in the DIC software were computed using the

common von Mises definition. While sufficient for isotropic materials, ZEK100-O magnesium alloy does not obey the von Mises yield criterion which is also the case for other magnesium alloys such as AZ31B (Ghaffari Tari *et al*., 2015). However, an anisotropic equivalent strain measure requires knowledge of the appropriate yield function and its coefficients which are not known in advance since the objective of the tensile and shear tests is to characterize anisotropy. The von Mises equivalent strain measure is a convenient, albeit simplistic, approximation for ZEK100-O with the advantage that no anisotropy coefficients or material parameters are required. For this reason, correlations for the stress and strain responses in this work are developed so that the interested reader can re-cast them in terms of the stress and plastic work for use in selecting and calibration of an appropriate yield function. The relevant equations to determine the shear strain components are presented in the subsequent sections.

3.6. Mechanics of Shear Deformation

For a finite level of shear deformation, γ (ratio of the shear displacement over the shear region width), applied in the x_1-x_2 plane, the deformation gradient, F_{ij}, rotation tensor, R_{ij}, logarithmic strain tensor, ε_{ij}, and stress tensor, σ_{ij} have been expressed by Onaka (2010) as:

$$F_{ij} = \begin{bmatrix} 1 & \gamma \\ 0 & 1 \end{bmatrix} \qquad R_{ij} = \frac{2}{\sqrt{4+\gamma^2}} \begin{bmatrix} 1 & \gamma \\ -\gamma & 1 \end{bmatrix} \tag{2,3}$$

$$\varepsilon_{ij} = \frac{\sinh^{-1}(\gamma/2)}{\sqrt{4+\gamma^2}} \begin{bmatrix} \gamma & 2 \\ 2 & -\gamma \end{bmatrix} \qquad \sigma_{ij} = \begin{bmatrix} \sigma_{11} & \tau_{12} \\ \tau_{12} & \sigma_{22} \end{bmatrix} \tag{4,5}$$

where the stress tensor includes normal stress components that develop with deformation and are related to the adopted constitutive model and objective stress rate. The principal logarithmic strains, ε_{1-3}, can be readily determined as:

$$\varepsilon_1 = -\varepsilon_2 = \sinh^{-1}\left(\frac{\gamma}{2}\right) \qquad \varepsilon_3 = 0 \tag{6}$$

For a von Mises material, the expression for the equivalent strain in shear loading reduces to:

$$\varepsilon_{eq} = \frac{2}{\sqrt{3}}\ \varepsilon_1 \tag{7}$$

The logarithmic strain equations in Eq. (4) and (5) revert to their familiar infinitesimal forms when the applied shear deformation is small:

$$\varepsilon_{ij} = \begin{bmatrix} 0 & \gamma/2 \\ \gamma/2 & 0 \end{bmatrix} \qquad \sigma_{ij} = \begin{bmatrix} 0 & \tau_{12} \\ \tau_{12} & 0 \end{bmatrix} \tag{8}$$

$$\varepsilon_1 = -\varepsilon_2 = \varepsilon_{12} = \frac{\gamma}{2} \qquad \varepsilon_{eq} = \frac{\gamma}{\sqrt{3}} = \frac{2\varepsilon_{12}}{\sqrt{3}} \tag{9}$$

The infinitesimal strain assumption is generally reasonable for many commercial sheet alloys. For example, the percent difference between the principal strains computed using Eq. (6) and Eq. (9) is less than 1% at an equivalent strain of 10%, only 2% at 40% strain and about 8% at 80% strain. Fortunately, the local DIC logarithmic strain measurements are valid for large strains and no assumptions are required to obtain ε_1 and ε_2. The infinitesimal strain assumption is only used to compute the shear stress response which assumes that the normal stress components in Eq. (5) remain negligible compared to the shear stress.

4. Results and Discussion

4.1. Uniaxial Tensile Response

The true stress response of ZEK100-O for uniaxial tension along the RD, DD, and TD directions is presented in Figure 8. Note that as mentioned earlier, at least four repeats were performed for each testing conditions while only a representative curve is shown in this section and it was observed that the deviations of experimental data are within a 2% band. The strong anisotropy of ZEK100-O is evident in Figure 8 as the initial yielding points and hardening rates are dependent upon the material orientation. Note that, recently, Min *et al.* (2014) performed uniaxial tensile tests in the TD direction of ZEK100 (O- and F-tempers) under different quasi-static strain rates and reported Yield Point Elongation (YPE) phenomenon and Portevin-Le

Châtelier (PLC) effects that increased with reducing the strain rates. However, these features were not observed in the response of ZEK100-O alloy considered in the present study.

The Lankford coefficient (r-value) is also a measure of the plastic anisotropy of a material subjected to uniaxial tension. The instantaneous r-values (r) are defined as:

$$r = \frac{\dot{\varepsilon}_2^p}{\dot{\varepsilon}_3^p} \tag{10}$$

where $\dot{\varepsilon}_2^p$ and $\dot{\varepsilon}_3^p$ correspond to the plastic thickness and width strain rates and are computed until the onset of necking. Note that a smoothing spline, available in Matlab®, was used to smooth the strain data before taking the numerical derivative to compute the instantaneous r-values. The instantaneous r-values obtained in the RD, DD, and TD directions of ZEK100-O are presented in Figure 9 and their variation suggests an evolution of the material texture with deformation. Kurukuri *et al*. (2014a) did show that ZEK100-F exhibits a strong evolution of texture with deformation, largely due to twin reorientation, under uniaxial loading and that the activated deformation mechanisms (slip *versus* twinning) were a function of load orientation with respect to initial texture. It is worth mentioning that the tensile data (true stress and instantaneous r-values) of ZEK100-O in Figures 8 and 9 were plotted until the onset of necking which is also a function of material orientation.

The uniaxial compression response of ZEK100-O is shown in Figure 8. The anisotropic behaviour of the material in compression is evident in the figure and it can be seen that ZEK100-O exhibits a tension-compression asymmetry. The sigmoidal shape of the stress response in compression is due to the activation of twinning mechanisms to accommodate plastic deformation. Although, ZEK100-O has higher ductility at room temperature compared to the more common variant, AZ31B-O, due to its relatively weaker basal texture (Kurukuri *et al*., 2014a), the results presented in Figures 8 and 9 show the challenging nature of ZEK100-O in terms of modelling and characterization with its significant anisotropy that evolves with deformation.

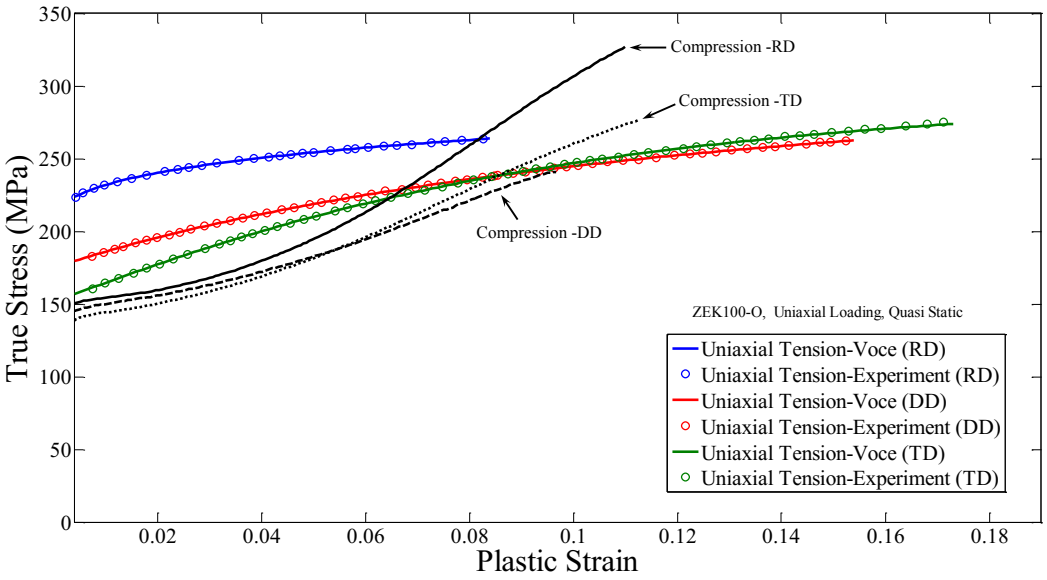

Figure 8 – True stress vs. plastic strain of ZEK100-O compared with predictions of Eq. (11).

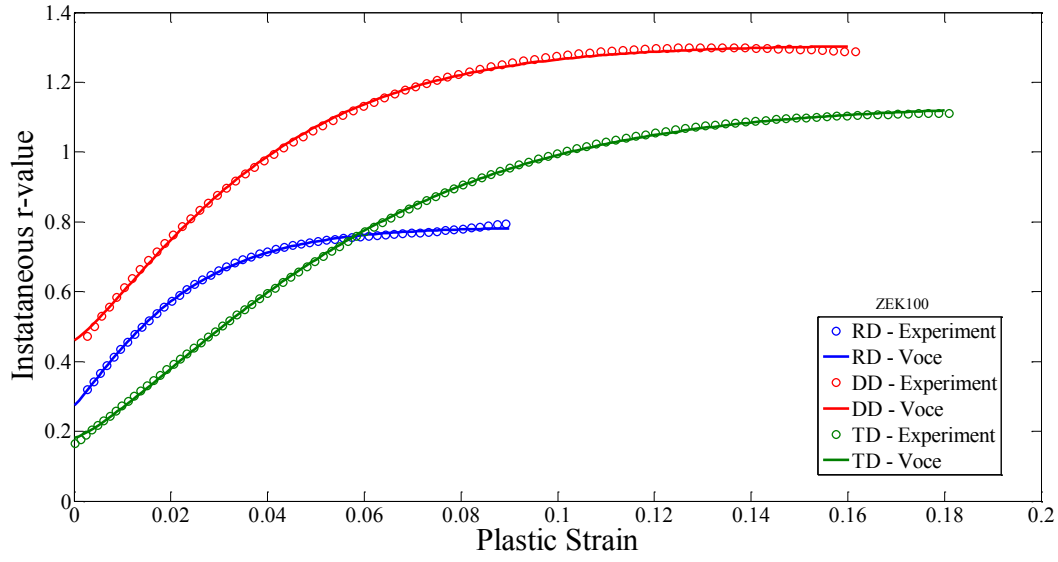

Figure 9 – Evolution of the instantaneous r-values of ZEK100-O with respect to plastic strain compared with predictions of Eq. (12).

In order to characterize the constitutive behaviour in tension, Hockett-Sherby functions (Hockett and Sherby, 1975) were fit to the measured true stress-plastic strain results up to the necking points of ZEK100-O:

$$\sigma = A + B\left[1 - \exp\left(-C\,(\varepsilon^p)^D\right)\right] \tag{11}$$

where A, B, C, and D are coefficients and ε^p is the plastic strain, were fit to each material direction. Note that "A" in Eq. (11) corresponds to the initial yield stress and "A+B" corresponds to the saturation stress. Table 3 presents the coefficients of Eq. (11) for ZEK100-O and the corresponding curves are compared with experimental results in Figure 8 and exhibit good agreement.

A similar algebraic equation to that of Eq. (11) was used to fit the instantaneous r-values as a function of plastic strain:

$$r = r_s + r_y\left[1 - \exp\left(-E(\varepsilon^p)^F\right)\right] \tag{12}$$

with calculated coefficients of r_y, r_s, E, and F that are presented in Table 4. The fit to Eq. (12) is compared to the experimental results in Figure 9 which shows good agreement. Using the coefficients of Tables 3 and 4, highly accurate fits with average R^2 values of 0.994 were obtained.

Table 3 – Coefficients of Eq. (11) for the flow stress of ZEK100-O.

Material	***A* (MPa)**	***B* (MPa)**	***C***	***D***	R^2
ZEK-RD	205.59	126.60	1.91	0.46	0.991
ZEK-DD	167.75	165.33	3.55	0.75	0.995
ZEK-TD	146.79	169.12	7.52	0.92	0.994

Table 4 – Coefficients of Eq. (12) for the instantaneous r-values of ZEK100-O.

Material	r_y	r_s	***E***	***F***	R^2
ZEK-RD	0.28	0.79	79.48	1.15	0.996
ZEK-DD	0.46	1.31	51.37	1.23	0.994
ZEK-TD	0.18	1.14	37.71	1.30	0.996

4.2. Shear Stress Response in Quasi-static Condition

Figure 10 shows the measured DIC contours and distributions of shear strain in the mini-shear specimen. As apparent from Figure 10, the shear strain is concentrated in the gauge area and is relatively uniform. Note that recently, Abedini *et al*. (2015) compared strain distributions of the mini-shear specimen versus a butterfly-type specimen and reported that the strains are more uniform in the gauge area of the mini-shear specimen.

It is important to mention that there will be some amount of rotation of the shear bands in these shear tests that might influence the behaviour of anisotropic materials. The rotation increases with deformation; therefore, it is more pronounced for higher strains and materials with high ductility. The rotation of the principal stretching direction can be determined using Mohr's circle as:

$$\beta = \frac{1}{2}\tan^{-1}\left(\frac{2}{\gamma}\right) \tag{13}$$

where β is the principal stretch angle. From the measured DIC strains for ZEK100-O, the maximum shear strain at failure was about 0.2 which corresponds to a rotation of the shear band of about 5.5°.

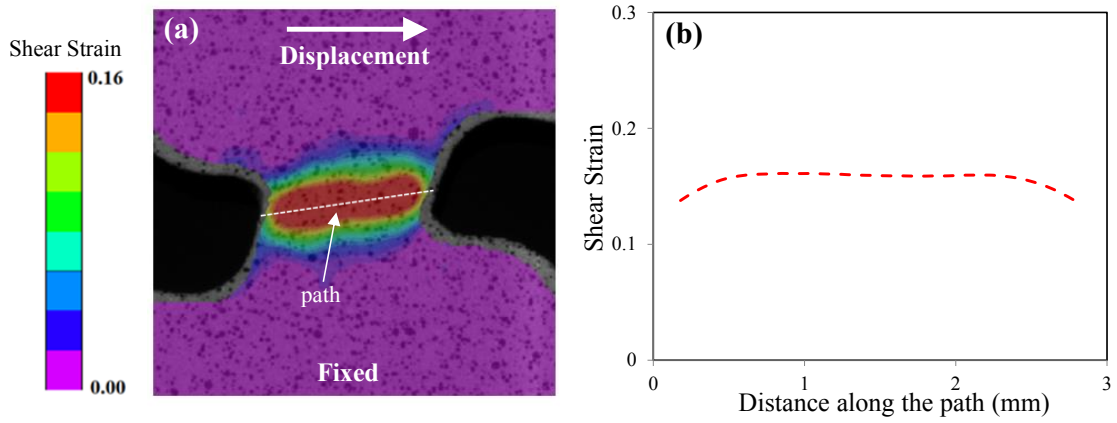

Figure 10 – (a) Contours of the shear strain and (b) distribution of shear strain in the gauge area for ZEK100-O in 90° orientation obtained with the DIC method.

Figure 11 shows the load-displacement response obtained with the mini-shear specimen for ZEK100-O. All of the experimental results show an initially linear response followed by an increasing load until fracture. The results of Figure 11 show that the sample in the 45° orientation undergoes the largest load at the time of yielding. In addition, the 135° orientation tests resulted in the lowest displacement to failure. Similar to the uniaxial tests, it was observed that the deviations of the experimental data are within a 2% band; therefore, only a representative curve is shown here.

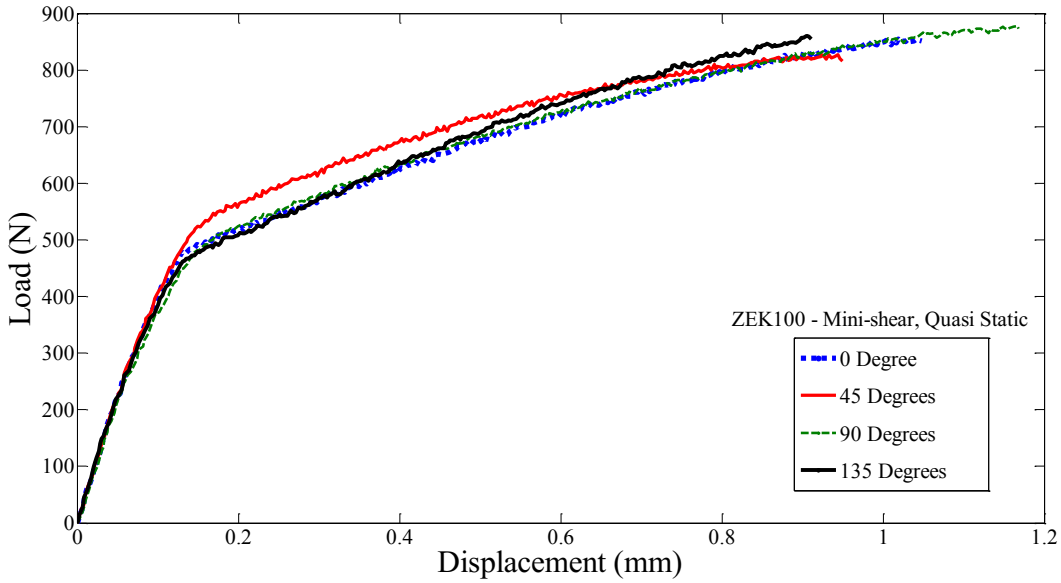

Figure 11 – Load *versus* displacement response of ZEK100-O mini-shear specimens.

It can be seen from Figure 11 that the results of the tests in 0° and 90° directions for ZEK100-O are almost identical in terms of the load-displacement response while the elongation to failure is slightly higher for the 90° orientation. The reason behind similar load response in 0° and 90° directions can be explained by considering an ideal shear loading condition where the principal loading directions are offset by 45° relative to the applied shear loading direction with equal and opposite magnitudes. The Mohr's circles for applied shear loadings in the 0, 45°, 90° and 135° directions are presented in Figure 12 to demonstrate the principal stress magnitudes and

directions and how these act on the various material directions for each load orientation. For example, for the experiments with the applied load in the rolling direction (0°), the tensile component of the principal stress is in the 45° direction while the compressive component is in the 135° direction. The opposite condition holds for the shear tests loaded in the 90° orientation where the principal stress in the 45° direction is compressive and the principal stress in the 135° direction is tensile (see conditions 1 and 3 in Figure 12). If the material is assumed to be orthotropic, and texture measurements support this assumption for ZEK100-O, the material will have the same tensile/compressive properties in the 45° and 135° directions, and as a result, the shear response in 0° and 90° orientations should be identical.

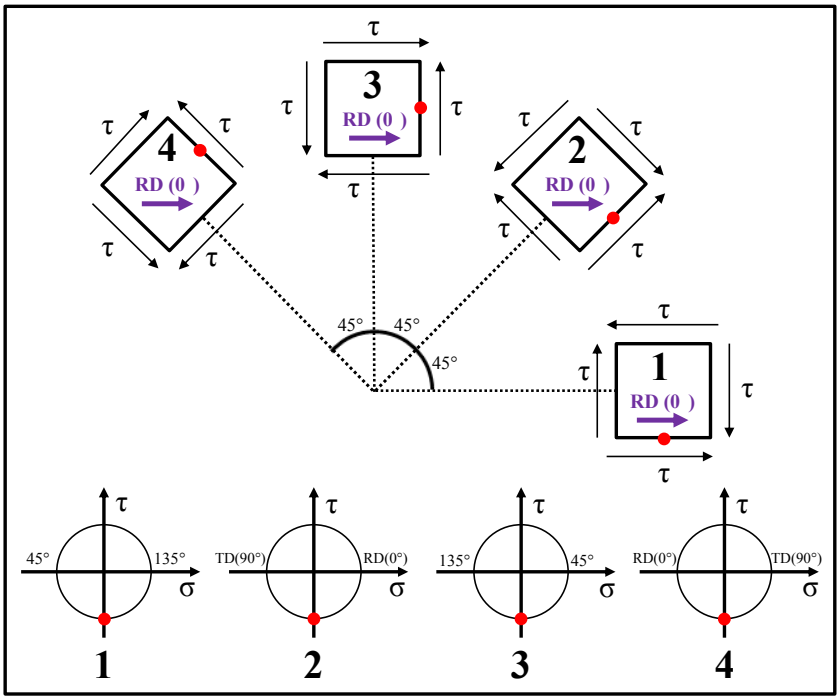

Figure 12 – Shear testing directions with their corresponding Mohr's circles. It was assumed that the shear in the clock-wise direction is positive.

When one considers the principal directions of the shear tests loaded in the 45° and 135° orientations, the tests in the 45° direction have a principal tensile component at 0° and a compressive component at 90°, whereas the shear tests in the 135° direction have a principal

compressive component in 0° and a tensile component at 90° (see conditions 2 and 4 in Figure 12). As shown above in Figure 8, ZEK100-O possesses a strong tension-compression asymmetry so that the response of the material in the rolling (0°) and transverse (90°) directions are significantly different in tension *versus* compression leading to the remarkable difference in the shear response of the material when loaded in the 45° *versus* the 135° directions. The above explanation is the reason for the difference in the load-displacement response between the 45° and 135° directions shown in Figure 11. The principal stress directions and magnitudes are the same but the signs of the principal stresses are opposite which triggers the asymmetric response of the material.

Therefore, shear tests in both the 45° and 135° orientations should be conducted for materials with tension-compression asymmetry to have a better understanding of the material behaviour. Furthermore, the principal stresses for tests in the 45° and 135° directions are located within the 2^{nd} and 4^{th} quadrants of a yield locus which are useful for the selection and calibration of an anisotropic yield function. For anisotropic materials that do not exhibit tension-compression asymmetry, shear tests are only required in two directions (0° or 90° and either 45° or 135°) (Lopes *et al*., 2003) since the 45° and 135° directions would result in the same response. Due to the fact that ZEK100-O exhibits both anisotropy and tension-compression asymmetry, the results of the shear tests performed with the applied load in the 45°, 90°, and 135° orientations are required and are presented for the remainder of the paper. Further discussions regarding the asymmetric response of the material are given in Section 4.3 using the CPB06 yield function.

Figure 13 shows the respective shear stress-strain responses of ZEK100-O obtained using Eq. (1) and the measured DIC strain data. The shear strains were obtained by averaging the measured DIC shear strains at the center of the gauge area as explained in Section 3.5. Additional information on the procedure for the extraction of the average shear strains in the gauge area using DIC is discussed in Peirs *et al*. (2012) and in detail by Rahmaan *et al*. (2015).

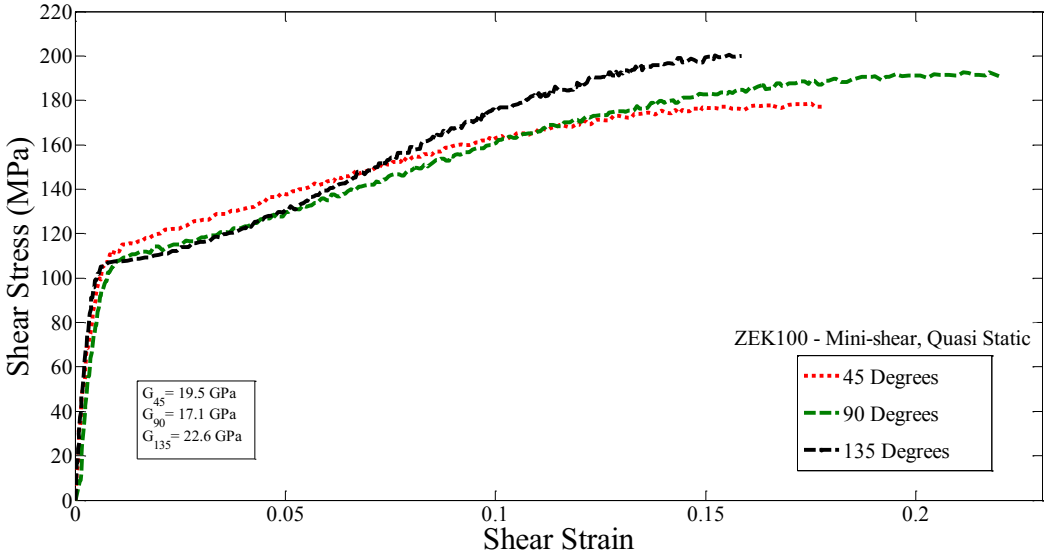

Figure 13 - Average shear stress-shear strain response calculated with the mini-shear specimen for ZEK100-O (*G* is the shear modulus of the material).

The results of Figure 13 show the strong anisotropy of ZEK100-O alloy when undergoing shear deformation. Furthermore, the hardening response of the sample in 135° exhibits a sigmoidal extension twinning signature. This behaviour is also observed for the 90° specimen but to a relatively lesser extent, while it is not exhibited by the 45° specimen. To explore this behaviour in greater detail, the microstructure of the deformed material was analyzed using EBSD and the results are shown in Section 4.2.1.

4.2.1. EBSD Analysis

In order to better explain the trends of the curves in Figure 13, the microstructure of the deformed material adjacent to the fractured surface of the mini-shear specimen was analyzed using EBSD. Inverse pole figure maps were obtained for the fractured samples over an area of 100µm × 200µm using a step size of 0.2µm. This fine step size was used in order to resolve twins within the shear bands.

Figure 14 shows the EBSD data for the 45°, 90° and 135° oriented shear samples in an area adjacent to the fracture surface. Figures 14(a-c) correspond to the inverse pole figure component maps while Figures 14(d-f) show the band contrast maps which highlight the various twin systems. A considerable amount of twinning is observed in all of the cases and the area percentages of the boundaries which have characteristic twin orientations are summarized in Table 5.

Sample 135° displays the largest fraction of twinning in the area of interest while Sample 45° exhibits the least amount of twinning. It has been established that Samples 135° and 90° show a defined twinning effect in the stress strain response (Figure 13). Channel die compression tests of magnesium single crystals with precise orientations have suggested that extension twins are primarily responsible for this twinning effect on the work hardening rate (Schmid and Boas, 1968; Kelley and Hosford, 1968). This twinning type is frequently observed in magnesium alloys due to its low critical resolved shear stress and accounts for the majority of the total twin boundaries in samples 135º and 90º. Furthermore, both samples exhibit similar percentages of the various twin systems. These samples have similar hardening behaviour; however, the work hardening rate of sample 135º is larger than that of sample 90º at larger strain values. This can be explained by the grain boundary strengthening effect. In the earlier stages of deformation, twins nucleate to accommodate strain incompatibilities (Barnett, 2007a). However, once nucleated the twins have effectively reduced the grain size and produced new boundaries which impede dislocation glide (Nemcko and Wilkinson, 2016). Sample 135º exhibits a larger fraction of twins and, therefore, has produced more boundaries to impede dislocation movement, hence the higher work hardening rate observed in this sample.

Furthermore, as explained in Section 4.2, shear stress in the 135º orientation leads to a compressive principal stress in the RD and a tensile principal stress in the TD. This type of loading favors extension twinning since the majority of grains in the microstructure of ZEK100-O are orientated with their c-axis parallel to the TD (see Section 2) so that the shear test in 135º orientation results in extension along c-axis and contraction normal to c-axis which is known to trigger extension twinning in magnesium alloys (Wu *et al.*, 2008).

In contrast, the twinning effect is not observed in the hardening rate of the 45° sample (Figure 13) in which the stress-strain response is dominated by compression and double twinning. It

should be noted that the orientation of this sample is such that the majority of the c-axes in the sample experience compression (the principal stress components are tensile in the RD and compressive in the TD, as shown in Figure 12). This sample contains the largest fraction of compression twins which have been argued to decrease the uniform elongation of magnesium alloys (Barnett, 2007b). Compression twinning occurs at large values of shear stress and often twinning along the $\{10\bar{1}1\}$ plane causes retwinning along $\{10\bar{1}2\}$ due to the reorientation of the c-axis and the low shear stress required to initiate twinning along this plane. Nevertheless, the EBSD observations suggest that the stress-strain responses can be directly related to the twin types and fractions of twins which form in the shear band. The results highlight the strong mechanical anisotropy of ZEK100-O as the samples loaded at 45º, 90º, and 135º with respect to the rolling direction exhibit different activities of the various deformation mechanisms. As a consequence, it is imperative that shear tests are carried out in the three orientations presented here to characterize the shear anisotropy of such materials.

Table 5 – Distribution of various twin types in the samples.

Twin Type	Area fraction of twin boundaries (Total percentage of twin boundaries)		
	Sample 45°	Sample 90°	Sample 135°
Extension Twin	0.047 (46)	0.059 (51)	0.070 (55)
Compression Twin	0.023 (22)	0.017 (15)	0.019 (15)
Double Twin	0.033 (32)	0.040 (34)	0.039 (30)
Total	0.103 (100)	0.116 (100)	0.128 (100)

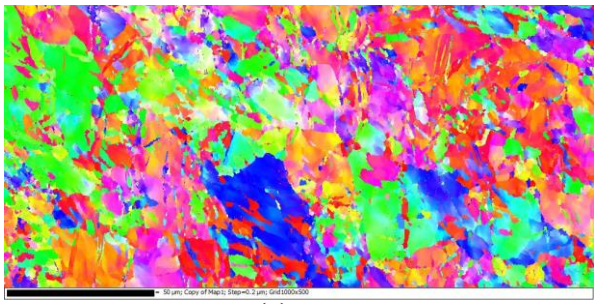

(a)

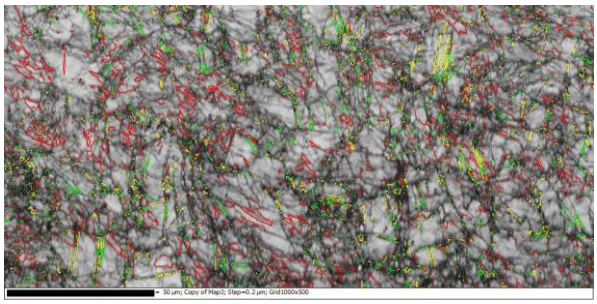

(d)

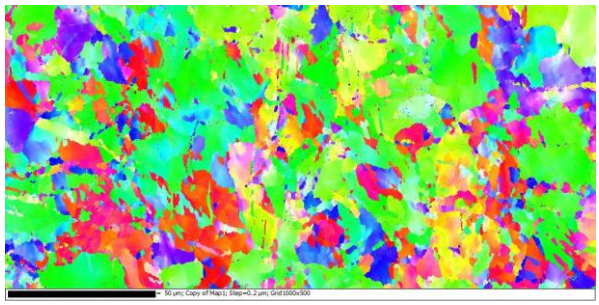

(b)

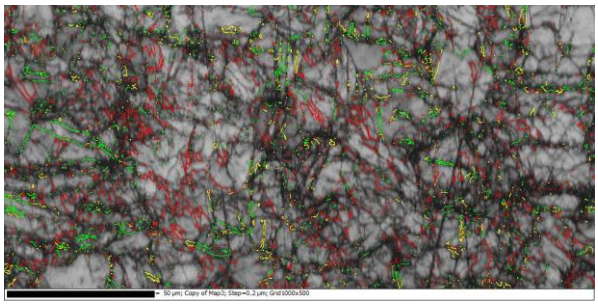

(e)

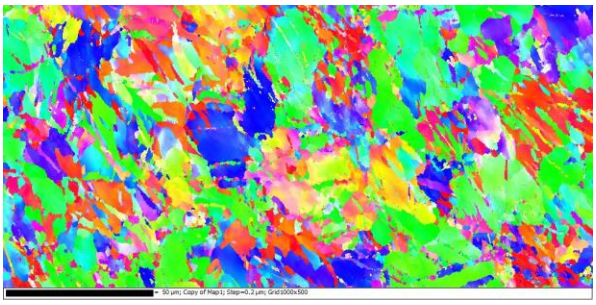

(c)

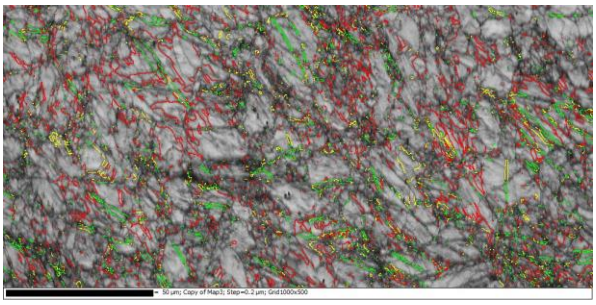

(f)

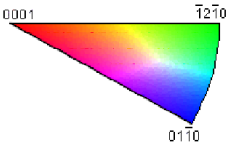

Twin Type	Twinning Plane	Misorientation Angle	
Extension Twin	$\{10\bar{1}2\}$	86° about $\langle 11\bar{2}0\rangle$	
Compression Twin	$\{10\bar{1}1\}$	56° about $\langle 11\bar{2}0\rangle$	
Double Twin	$\{10\bar{1}1\}-\{10\bar{1}2\}$	38° about $\langle 11\bar{2}0\rangle$	

Figure 14 - EBSD data showing the inverse pole figure component maps for samples (a) 45°, (b) 90° and (c) 135° as well as band contrast maps with the various twin systems highlighted for samples (d) 45°, (e) 90° and (f) 135°. Note that the specimens were analyzed after the onset of fracture.

It is important to emphasize that, in the present work, activations of twinning mechanisms were observed for a magnesium alloy with rare-earth elements; however, these activations are

due to the HCP crystal structure and preferred orientation of grains. In order to illustrate this better, shear tests similar to those considered for the current ZEK100-O were performed on a more common magnesium alloy sheet, AZ31B-O, and the results are shown in Figure 15. The sigmoidal trends are apparent in Figure 15; however, as opposed to the response of the ZEK100-O, the twinning plateau exists in the shear stress-strain curves of AZ31B-O in all three directions. Also compared to ZEK100-O, the shear response of AZ31B-O exhibits a less pronounced orientation-dependency. These facts can be attributed to the texture of the AZ31B-O, as reported in Kurukuri *et al.* (2014b), in which the majority of grains are orientated with their c-axis parallel to the normal direction of the sheet with only a minor spreading towards the sheet RD. As a result of the AZ31B texture, in-plane shear loadings in different orientations are similarly favorable for extension twinning.

To compare the shear responses of ZEK100-O and AZ31B-O, the stress-strain curves shown in Figures 13 and 15 were normalized by their initial yield stress and the results are shown in Figure 16. It can be seen that the work hardening rates for shear tests on AZ31B-O are higher than that of ZEK100-O. Furthermore, it can be observed from Figure 16 that ZEK100-O has higher ductility in shear loading, although the anisotropic behaviour of ZEK100-O is remarkably more severe than AZ31B-O. More information regarding tensile and compressive constitutive behaviour of AZ31B-O can be found in Kurukuri *et al*. (2014b).

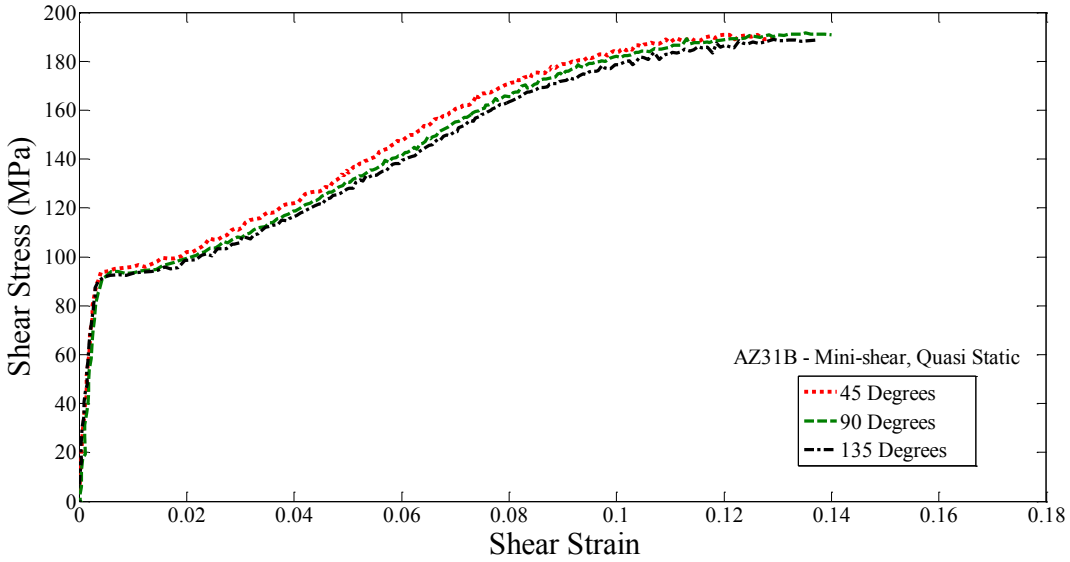

Figure 15 - Average shear stress-shear strain response calculated with the mini-shear specimen for AZ31B-O.

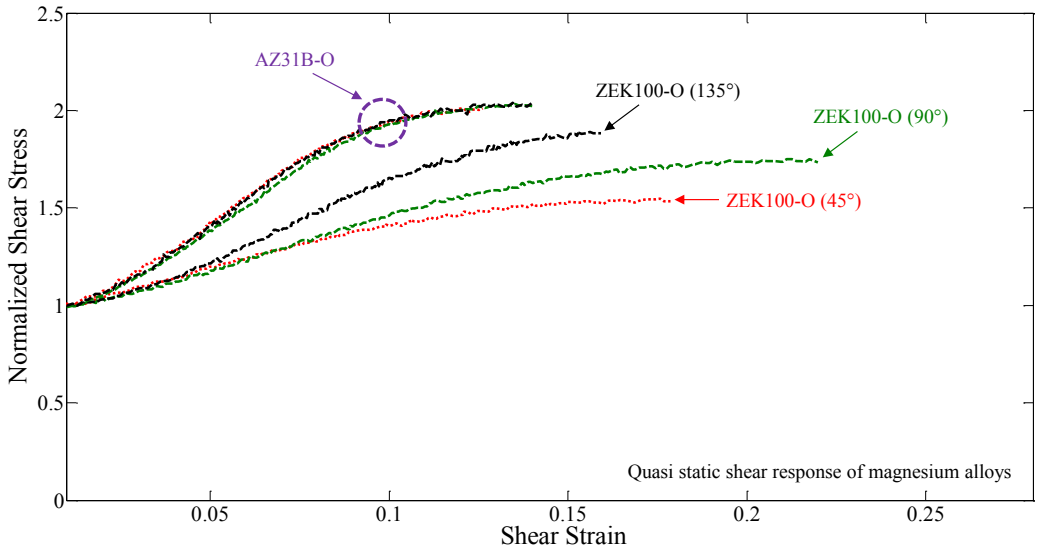

Figure 16 - Normalized shear stress-shear strain response of magnesium alloys ZEK100-O and AZ31B-O.

4.3. Anisotropic and Asymmetric Yield Loci

The ultimate goal for extensive anisotropic characterization is generally to calibrate anisotropic yield criteria to describe the behaviour of materials in finite element simulations. The complex anisotropic behaviour and evolving anisotropy of ZEK100-O is challenging and an advanced anisotropic yield criterion is required. Therefore, in order to better evaluate some of the experimental trends observed in Section 4.2, the CPB06 phenomenological yield criterion proposed by Cazacu *et al.* (2006) was adopted in the present study to investigate the yield locus of ZEK100-O. In analogy to Plunkett *et al.* (2008), two stress transformations were performed to increase the degree of flexibility of the model (denoted as CPB06ex2). The yield function, φ, is defined as:

$$\varphi = (|\Sigma_1| - k\Sigma_1)^a + (|\Sigma_2| - k\Sigma_2)^a + (|\Sigma_3| - k\Sigma_3)^a + (|\Sigma'_1| - k'\Sigma'_1)^a + (|\Sigma'_2| - k'\Sigma'_2)^a + (|\Sigma'_3| - k'\Sigma'_3)^a \quad (14)$$

where k and k' are material parameters that account for strength differential effects, and a is the exponent of the yield function. Also $\Sigma_1, \Sigma_2, \Sigma_3$ and $\Sigma'_1, \Sigma'_2, \Sigma'_3$ are the principal values of the transformed stress deviators Σ_{ij} and Σ'_{ij} written as:

$$\Sigma_{ij} = C_{ijkl} : S_{kl} \quad \text{and} \quad \Sigma'_{ij} = C'_{ijkl} : S_{kl} \quad (15,16)$$

where S_{kl} is the deviatoric stress tensor and the fourth-order transformation tensors C_{ijkl} and C'_{ijkl} are given by:

$$C_{ijkl} = \begin{bmatrix} C_{11} & C_{12} & C_{13} & & & \\ C_{12} & C_{22} & C_{23} & & & \\ C_{13} & C_{23} & C_{33} & & & \\ & & & C_{44} & & \\ & & & & C_{55} & \\ & & & & & C_{66} \end{bmatrix} \quad \text{and} \quad C'_{ijkl} = \begin{bmatrix} C'_{11} & C'_{12} & C'_{13} & & & \\ C'_{12} & C'_{22} & C'_{23} & & & \\ C'_{13} & C'_{23} & C'_{33} & & & \\ & & & C'_{44} & & \\ & & & & C'_{55} & \\ & & & & & C'_{66} \end{bmatrix} \tag{17,18}$$

The values of coefficients of the transformation tensors and strength differential parameters (k and k') can be determined from an optimization approach to minimize the errors between the experimental data and the values predicted by the yield function. In the present study, the genetic algorithm (GA) which is a global optimizer available in Matlab® was used to minimize "*Error*" given by:

$$Error = w_\sigma \sum_{i=1}^{n_1} \left(\left(\frac{\sigma^t_{CPB}}{\sigma^t_{\exp}} \right)_i - 1 \right)^2 + w_\sigma \sum_{i=1}^{n_2} \left(\left(\frac{\sigma^c_{CPB}}{\sigma^c_{\exp}} \right)_i - 1 \right)^2 + w_\sigma \sum_{i=1}^{n_3} \left(\left(\frac{\tau_{CPB}}{\tau_{\exp}} \right)_i - 1 \right)^2 + w_r \sum_{i=1}^{n_4} \left(\left(\frac{r^t_{CPB}}{r^t_{\exp}} \right)_i - 1 \right)^2 \tag{19}$$

where n_1, n_2, and n_3 are the number of available tensile, compressive, and shear stresses, respectively, and n_4 is the number of r-values. In this paper, the values of n_1, n_2, n_3, and n_4 are equal to three due to the fact that the experimental tests were performed in three orientations of the sheet. Furthermore, the superscripts t and c show tension and compression values, respectively, and the superscripts *exp* and *CPB* show whether the values are from experiments or from the CPB06ex2 yield function. In addition, w_σ and w_r are the weighting values for stresses and r-values where $w_\sigma = 0.9$ and $w_r = 0.1$ were used.

In the present study, the experimental values corresponding to three levels of plastic deformation were considered for calibrating the yield function. Three plastic work levels of 2.24 MPa, 14.61 MPa, and 22.46 MPa were considered that correspond to true plastic strains of 0.01, 0.06, and 0.09, respectively, for a uniaxial tension test in the rolling direction. Note that magnesium alloys exhibit an evolving anisotropy in which the shape of the yield locus continuously evolves with plastic deformation; however, in order to assist with the arguments

made in Section 4.2, fitting of the yield locus was only performed at these discrete levels of plastic deformation. The resulting coefficients of the CPB06ex2 criterion are given in Table 6 and the corresponding yield loci are shown in Figures 17-19. The yield loci in Figures 17-19 are plotted in two different planes with axes of normalized stress in 0° (RD) and 90° (TD) in Figures 17a, 18a, and 19a, and axes of normalized stress in 45° and 135° orientations in Figures 17b, 18b, and 19b. The red circles in Figure 17-19 show the experimental values used for calibrating the yield function.

It can be seen from Figures 17-19 that the CPB06ex2 yield criterion fits the measured data with good accuracy. For the small plastic work level of 2.24 MPa which is close to the initial yielding of the material, it can be seen from Figure 17 that the material has a clear tension-compression asymmetry with the tension region having larger yield stresses than the compression region. The tension-compression asymmetry of yield loci reduces with deformation as shown in Figure 18 for the plastic work level of 14.61 MPa while as shown in Figure 19 for the plastic work level of 22.46 MPa, the yield stresses in compression are larger than in tension which is opposite to that observed for the material at the onset of yielding.

Furthermore, it can be seen that an additional asymmetry exists in the 2^{nd} and 4^{th} quadrants of the yield loci in Figures 17a, 18a, and 19a where the shear yield stresses acting along the 45° and 135° orientations are located. Interestingly, this shear asymmetry does not exist in Figures 17b, 18b, and 19b in the regions of shear yield stresses acting in the 0° and 90° orientations. This behaviour confirms the statements made in Section 4.2 using arguments based upon a Mohr's circle visualizations of the principal stress directions in the shear tests. The shear asymmetry captured in Figures 17a, 18a, and 19a emphasizes the importance of performing shear tests with the applied load in the three orientations of 0° (or 90°), 45°, and 135° with respect to the rolling direction for orthotropic sheet metals exhibiting tension-compression asymmetry.

Table 6 – Coefficients of CPB06ex2 for ZEK100-O alloy. Exponent of a=8 was used for calibration of the yield function. Note that the anisotropy coefficients associated with the out of plane shears (C_{44}, C_{55}, C'_{44}, C'_{55}) were not calibrated due to the lack of experimental results.

Plastic Work (MPa)	2.24	14.61	22.46
C_{11}	1.0000	1.0000	1.0000
C_{12}	0.8062	0.7646	-0.4892
C_{13}	0.2684	0.3443	0.8834
C_{22}	0.2200	0.0373	1.0689
C_{23}	0.0891	0.0565	-0.5262
C_{33}	0.4504	0.4703	-0.4731
C_{66}	0.4773	0.7804	-1.4619
k	0.2026	0.0127	-0.2679
C'_{11}	1.0000	1.0000	1.0000
C'_{12}	0.6033	0.5007	1.5596
C'_{13}	1.0200	0.2267	1.2146
C'_{22}	-0.0210	-0.3226	1.6732
C'_{23}	0.8788	0.4792	-0.0966
C'_{33}	1.4957	-0.4258	-0.6971
C'_{66}	0.6117	0.7390	-1.8438
k'	-0.0670	0.0072	-0.0366

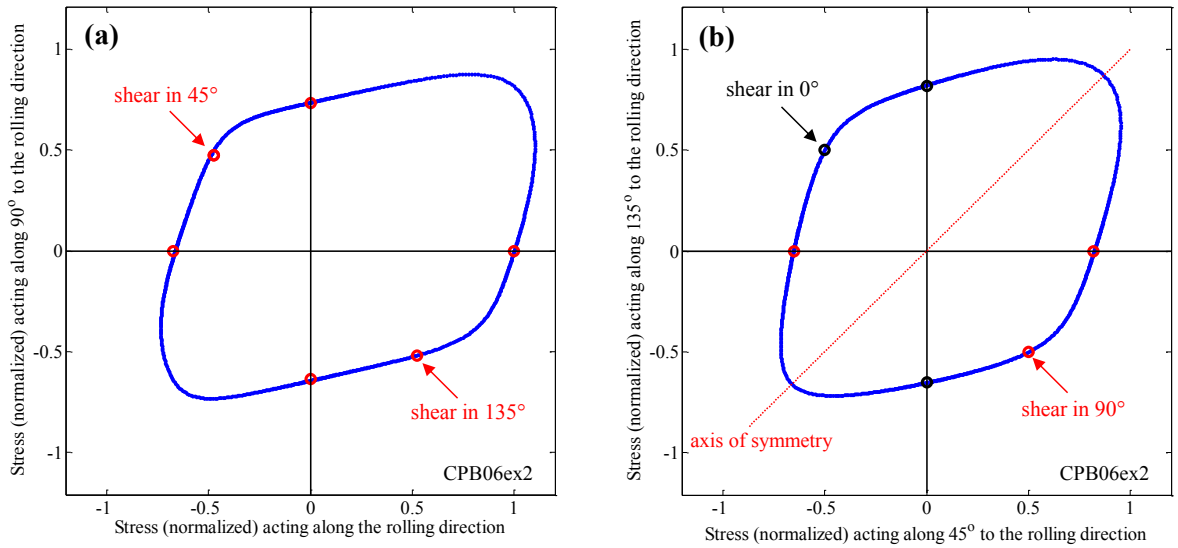

Figure 17 – Yield locus of ZEK100-O corresponding to a plastic work level of 2.24 MPa, plotted in the two planes with the axes of (a) normal stress acting in 0° and 90° to material rolling direction (normalized by yield stress for uniaxial tension along RD), and (b) normalized stress in 45° and 135° with respect to the rolling direction (normalized by yield stress for uniaxial tension along RD). The black circles show the experimental results where the red circles were used for calibrating the yield function.

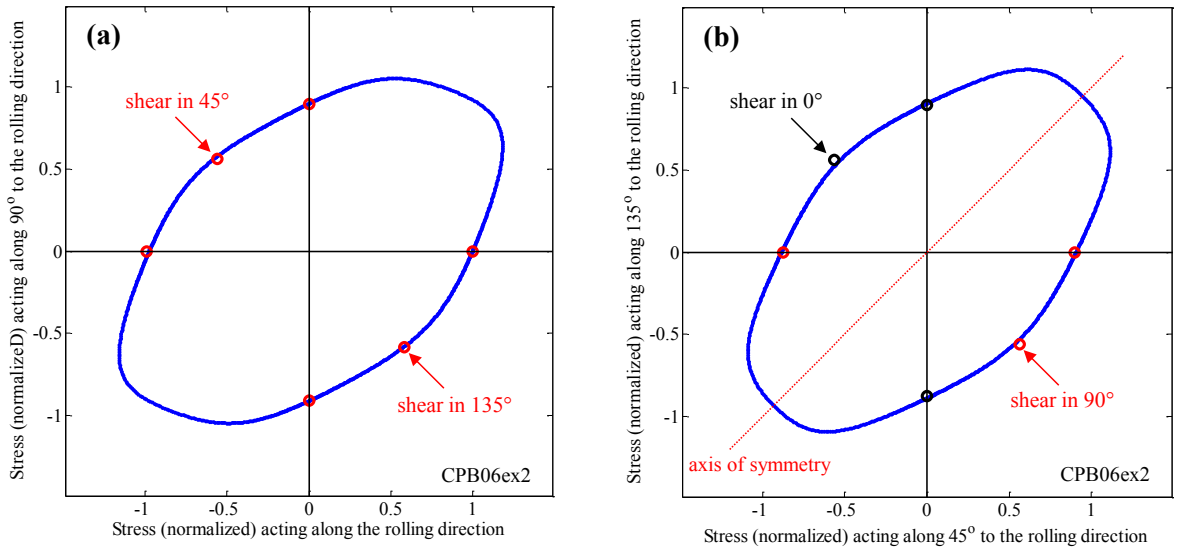

Figure 18 – Yield locus of ZEK100-O corresponding to a plastic work level of 14.61 MPa, plotted in the two planes with the axes of (a) normal stress acting in 0° and 90° to material rolling direction (normalized by yield stress for uniaxial tension along RD), and (b) normalized stress in 45° and 135° with respect to the rolling direction (normalized by yield stress for uniaxial tension along RD). The black circles show the experimental results where the red circles were used for calibrating the yield function.

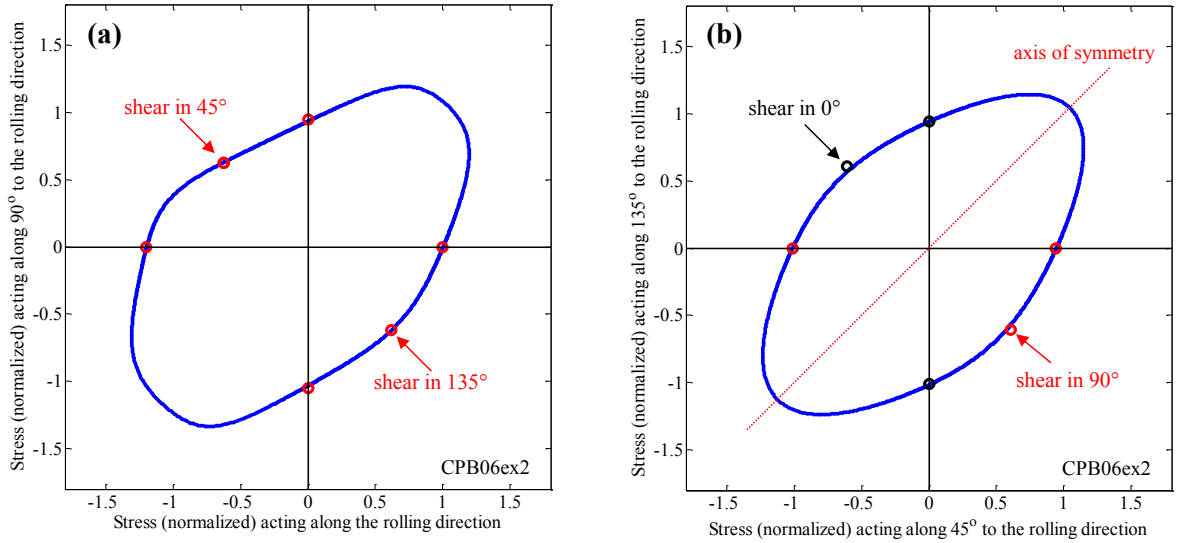

Figure 19 – Yield locus of ZEK100-O corresponding to a plastic work level of 22.46 MPa, plotted in the two planes with the axes of (a) normal stress acting in 0° and 90° to material rolling direction (normalized by yield stress for uniaxial tension along RD), and (b) normalized stress in 45° and 135° with respect to the rolling direction (normalized by yield stress for uniaxial tension along RD). The black circles show the experimental results where the red circles were used for calibrating the yield function.

4.4. Shear Stress Response at Elevated Strain Rates

The results of Sections 4.1-4.3 were based on shear tests under quasi-static conditions but it is instructive, specifically in terms of crashworthiness performance of materials, to evaluate the influence of strain rate on shear response. High-rate uniaxial tensile and compressive response of rare-earth magnesium alloys were previously studied by Kurukuri *et al.* (2014a) while the shear response has never been characterized at elevated rates. The effect of strain rate on the shear response of ZEK100-O is presented in Figure 20 with each material orientation exhibiting positive rate sensitivity. The hardening rates increase with strain rate while the shapes of the trends remain similar to those under quasi-static conditions suggesting that similar deformation mechanisms are active for the range of strain rates considered. For tests in the 45° and 90° orientations, the initial yield stress increases as the strain rate gets larger while the tests in the 135° direction show negligible rate sensitivity of the initial yield stress. This behaviour is consistent with earlier work reported by Kurukuri *et al.* (2014a) and Min *et al.* (2014) on

ZEK100-F which demonstrated that slip-dominated deformation modes exhibit positive rate sensitivity whereas twinning-dominated modes are rate-insensitive.

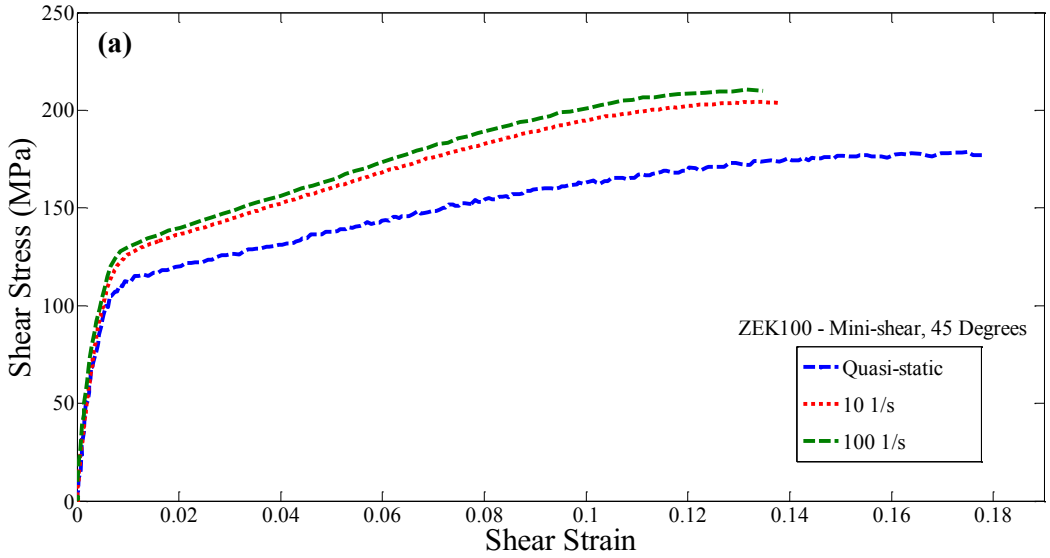

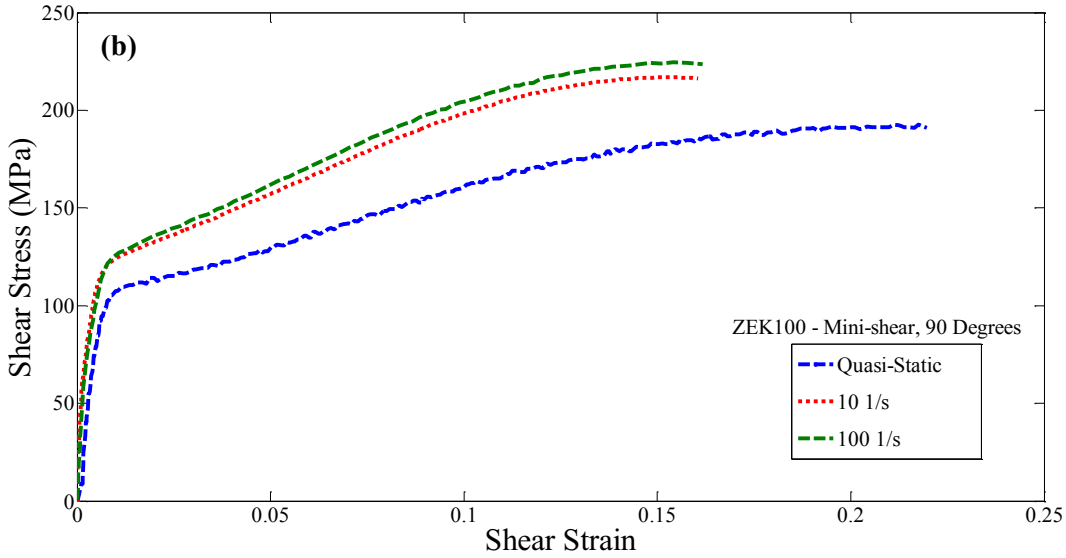

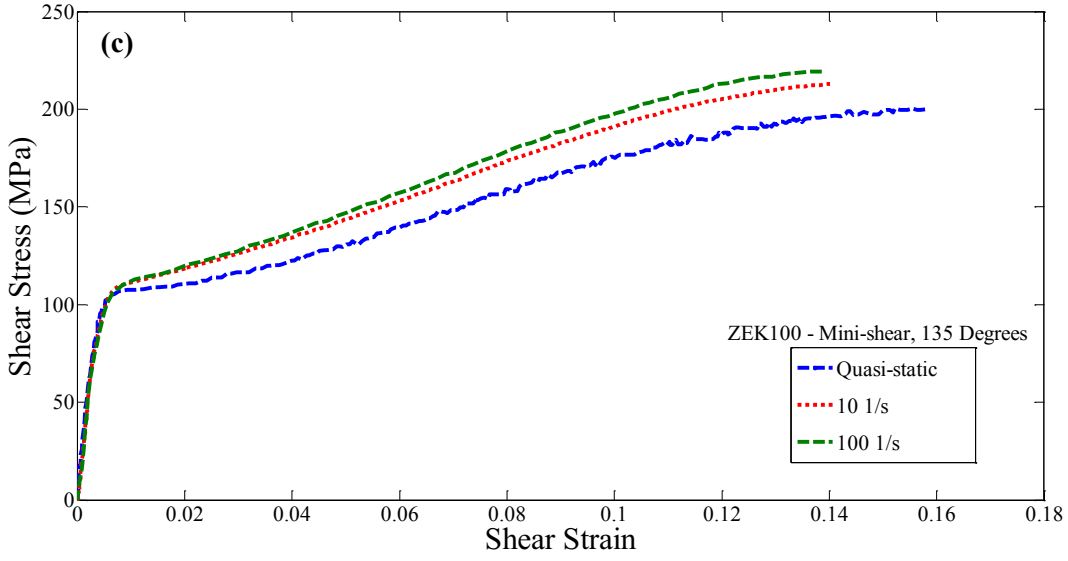

Figure 20 - Shear response of ZEK100-O obtained at different strain rates for (a) 45°, (b) 90°, and (c) 135° directions.

In order to enable adoption of the measured shear response of ZEK100-O in constitutive models, mathematical fits to the shear stress-strain data were developed. A strain-rate dependent constitutive model for the uniaxial compressive behaviour response of ZEK100-F was proposed by Kurukuri *et al*. (2014a). This model captures the strain rate-insensitive twinning plateau followed by rate sensitive hardening through plastic slip. By replacing the equivalent stress with the shear stress and the equivalent plastic strain for the plastic shear strain, the Kurukuri model can be expressed as:

$$\tau = \frac{\tau_y \alpha_1 + K(\varepsilon_{12}^p)^n \left[1 + \alpha_2 \ln(\dot{\varepsilon}/\dot{\varepsilon}_0)\right]^{-1}}{\alpha_1 + (\varepsilon_{12}^p)^n} \tag{20}$$

in which τ_y is the shear yield stress, $\dot{\varepsilon}_0$ is the reference strain rate of 0.01 s^{-1}, and α_1 , α_2, K, and n are material parameters. Also ε_{12}^p is the plastic shear strain defined by:

$$\varepsilon_{12}^p = \varepsilon_{12} - \frac{\tau}{2G} \tag{21}$$

where ε_{12} is the total shear strain and G is the shear modulus.

Yielding in Eq. (20) is independent of the strain rate since Kurukuri *et al.* (2014a) did not observe any rate dependency of yielding which is known to be twinning dominated for compressive loading. However, inspection of the results in Figure 20 indicates that the shear yield stress can be sensitive to the strain rate. Thus, an additional parameter, α_3, is added to Eq. (20) to obtain:

$$\tau = \frac{\tau_y \alpha_1 \left[1 + \alpha_3 \ln(\dot{\varepsilon}/\dot{\varepsilon}_0)\right] + K(\varepsilon_{12}^p)^n \left[1 + \alpha_2 \ln(\dot{\varepsilon}/\dot{\varepsilon}_0)\right]^{-1}}{\alpha_1 + (\varepsilon_{12}^p)^n} \tag{22}$$

The coefficients of Eq. (22) were determined using least-squares optimization procedure using a custom Matlab® script and are presented in Table 7. The resulting constitutive behaviour using Eq. (22) and the parameters in Table 7 are compared with the experimental results in Figure 21 showing good agreement with the measured data. The predicted shear stress-strain response at equivalent strain rates of $0.001 s^{-1}$ and $1000\ s^{-1}$ are also included in Figure 21 to show the extrapolation of the predictions under extreme rates of strain. It is recognized that the extrapolated predictions require validation as part of on-going work.

Table 7 – Coefficients of Eq. (22) for ZEK100-O.

Shear Loading Direction	τ_y **(MPa)**	K **(MPa)**	n	α_1	α_2	α_3	R^2
45°	107.35	280.94	1.015	0.1873	0.0159	-0.0245	0.991
90°	109.14	205.30	2.027	0.0058	0.0243	-0.0218	0.990
135°	104.44	250.25	1.869	0.0132	0.0104	-0.0137	0.991

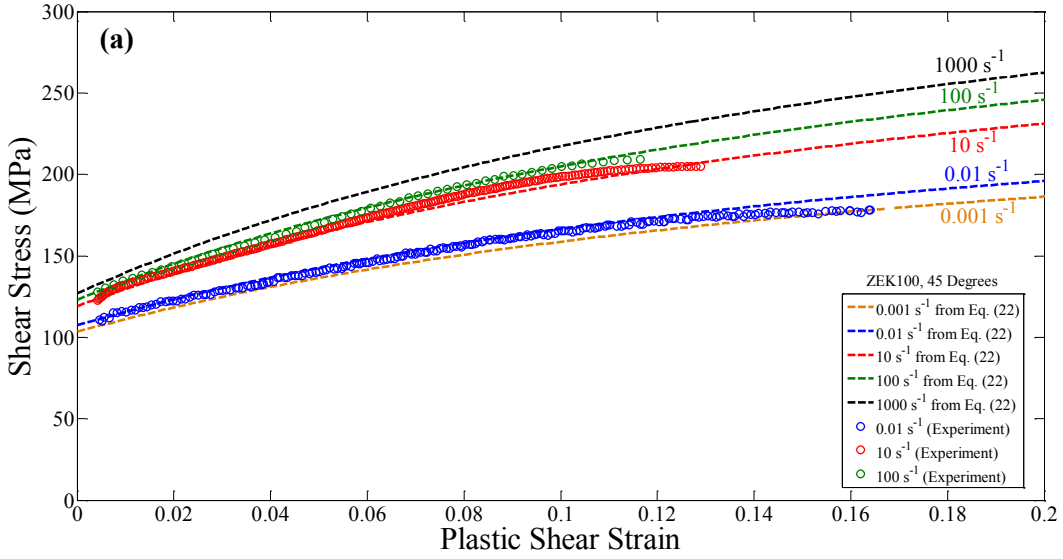
(a)
1000 s-1
100 s-1
10 s-1
0.01 s-1
0.001 s-1
ZEK100, 45 Degrees
0.001 s-1 from Eq. (22)
0.01 s-1 from Eq. (22)
10 s-1 from Eq. (22)
100 s-1 from Eq. (22)
1000 s-1 from Eq. (22)
0.01 s-1 (Experiment)
10 s-1 (Experiment)
100 s-1 (Experiment)
Shear Stress (MPa)
Plastic Shear Strain
0
50
100
150
200
250
300
0
0.02
0.04
0.06
0.08
0.1
0.12
0.14
0.16
0.18
0.2

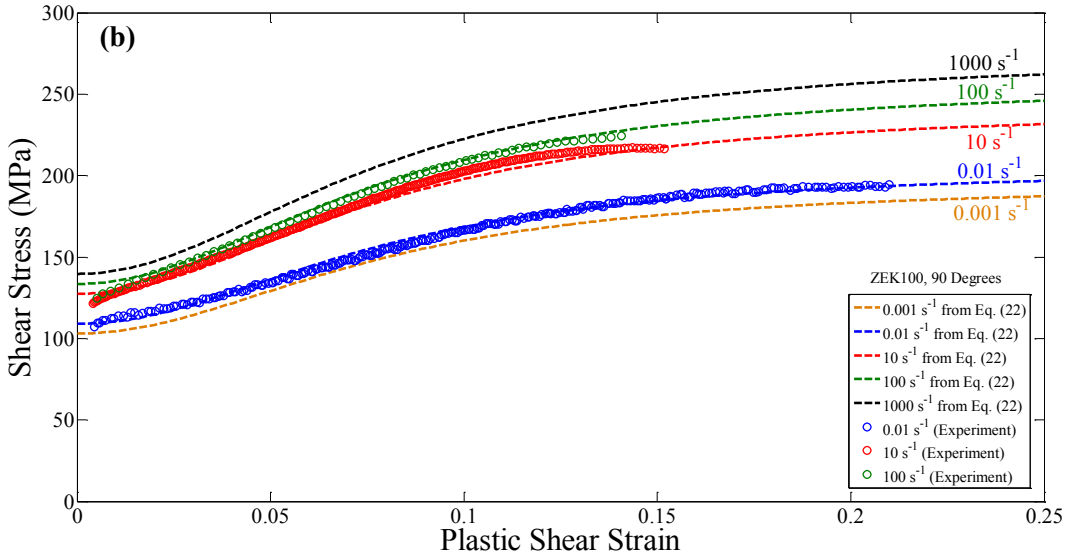
(b)
1000 s-1
100 s-1
10 s-1
0.01 s-1
0.001 s-1
ZEK100, 90 Degrees
0.001 s-1 from Eq. (22)
0.01 s-1 from Eq. (22)
10 s-1 from Eq. (22)
100 s-1 from Eq. (22)
1000 s-1 from Eq. (22)
0.01 s-1 (Experiment)
10 s-1 (Experiment)
100 s-1 (Experiment)
Shear Stress (MPa)
Plastic Shear Strain
0
50
100
150
200
250
300
0
0.05
0.1
0.15
0.2
0.25

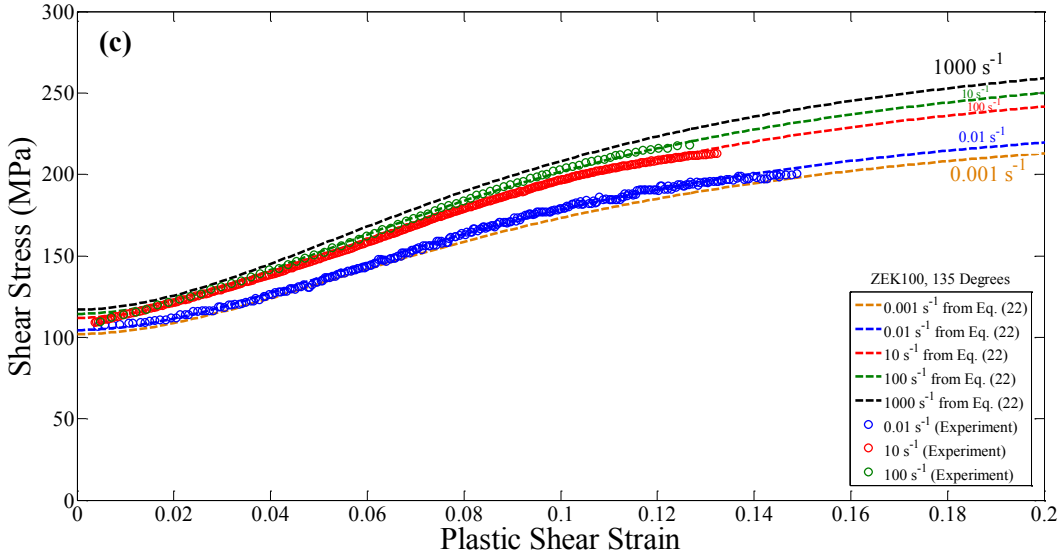

Figure 21 - Shear response obtained with experiments *versus* from Eq.(22) for ZEK100-O tested in (a) 45° (b) 90°, and (c) 135° directions.

5. Conclusions

The behaviour of a rare-earth magnesium alloy sheet (ZEK100-O) was examined in shear loading conditions at room temperature under quasi-static and elevated strain rates. The ZEK100-O alloy showed significant anisotropy in the shear stress-shear strain response; in addition, it was shown that shear tests in three different orientations of 0° (or 90°), 45°, and 135° with respect to the rolling direction are required to reveal the anisotropic behaviour and activation of different deformation mechanisms. The macroscopic shear stress response of ZEK100-O is strongly influenced by the activation of the various twinning modes in the HCP crystal structure, as confirmed by microstructural investigations using EBSD analysis. Furthermore, the CPB06ex2 yield function was calibrated with the experimental data from which the asymmetric response of the material in tension-compression and shear loading was evident in the calibrated yield loci. Finally, shear tests at elevated strain rates showed that the flow stress increases with increased strain rate where a rate-dependent constitutive model was proposed to account for the complex shear response of the material.

Acknowledgements

Financial support for this work provided by Cosma International, Automotive Partnership Canada, the Ontario Research Fund, the Natural Sciences and Engineering Research Council of Canada, the Canada Research Chairs Secretariat, and the Canada Foundation for Innovation is gratefully acknowledged.

References

Abedini A, Butcher C, Anderson D, Worswick M J, Skszek T (2015) Fracture characterization of automotive alloys in shear loading, SAE International Journal of Materials and Manufacturing, 8(3).

Abedini A, Butcher C, Worswick M J (2017) Fracture characterization of rolled sheet alloys in shear loading: Studies of specimen geometries, anisotropy, and rate sensitivity, Experimental Mechanics, 57:75-88.

Bae D G, Ghosh A K (2003) A planar simple shear test and flow behavior in a superplastic Al-Mg alloy. Metallurgical and Materials Transactions A, 34:2465-2471.

Bai Y, Wierzbicki T (2008) A new model of metal plasticity and fracture with pressure and Lode dependence. International Journal of Plasticity, 24:1071-1096.

Bai Y, Wierzbicki T (2010) Application of extended Mohr-Coulomb criterion to ductile fracture. International Journal of Fracture, 161:1-20.

Bardelcik A, Worswick M J, Wells M A (2014) The influence of martensite, bainite and ferrite on the as-quenched constitutive response of simultaneously quenched and deformed boron steel - Experiments and model, Materials and Design, 55:509-525.

Barnett M R (2007a) Twinning and the ductility of magnesium alloys, part I: "tension" twins, Materials Science and Engineering A, 464:1-7.

Barnett M R (2007b) Twinning and the ductility of magnesium alloys, part II: "contraction" twins, Materials Science and Engineering A, 464:8-16.

Bao Y B, Wierzbicki T (2004) On fracture locus in the equivalent strain and stress triaxiality space. International Journal of Mechanical Sciences, 46(1):81-98.

Bonnet-Lebouvier A S, Klepaczko J R (2002) Numerical study of shear deformation in Ti-6Al-4V at medium and high strain rates, critical impact velocity in shear. International Journal of Impact Engineering, 27(7):755-769.

Bouvier S, Haddadi H, Levee P, Teodosiu C (2006) Simple shear tests: Experimental techniques and characterization of the plastic anisotropy of rolled sheets at large strains. Journal of Materials and Technology, 172:196-103.

Brunig M, Chyra O, Albrecht D, Driemeier L, Alves M (2008) A ductile damage criterion at various stress triaxialities, International Journal of Plasticity, 24:1731-1755.

Cazacu O, Plunkett B, Barlat F, Orthotropic yield criterion for hexagonal closed packed metals, International Journal of Plasticity, 2006, 22:1171-1194.

Campbell J D, Fergusen W G (1970) The temperature and strain-rate dependence of the shear strength of mild steel, Philosophical Magazine, 21:169, 63-82.

Carbonniere J, Thuillier S, Sabourin F, Brunet M, Manach P Y (2009) Comparison of the work hardening of metallic sheets in bending-unbending and simple shear, International Journal of Mechanical Sciences, 51:122-130.

Dunand M, Mohr D (2011) On the predictive capabilities of the shear modified Gurson and the modified Mohr–Coulomb fracture models over a wide range of stress triaxialities and Lode angles. J Mechanics and Physics of Solids, 59:1374-1394.

Gao F, Gui L, Fan Z (2011) Experimental and numerical analysis of an in-plane shear specimen designed for ductile fracture studies. Experimental Mechanics, 51:891-901.

Gasperini M, Pinna C, Swiatnicki W (1996) Microstructure evolution and strain localization during shear deformation of an aluminum alloy. Acta Materialia, 44(10):4195-4208.

Ghaffari Tari D, Worswick M J, Ali U, Gharghouri M A (2014) Mechanical response of AZ31B magnesium alloy: Experimental characterization and material modeling considering proportional loading at room temperature, International Journal of Plasticity, 55:247-267.

Gruben G, Fagerholt E, Hopperstad O S, Borvik T (2011) Fracture characteristics of a cold-rolled dual-phase steel, European Journal of Mechanics A/Solids, 30:204-218.

Guo Y, Li Y (2012) A novel approach to testing the dynamic shear response of Ti-6Al-4V, Acta Mechanica Solida Sinica, (25:3):299-311.

Hockett J E, Sherby O D (1975), Large strain deformation of polycrystalline metals at low homologous temperatures, Journal of Mechanics of Physics and Solids, 23:87-98.

Hubnatter W, Merklein M (2008) Characterization of material behavior under pure shear condition, International Journal of Material Forming, 1:233-236.

Iosipescu N (1967) New accurate procedure for single shear testing of metals. Journal of Materials, 2:537-566.

Kang J, Wilkinson D S, Wu P D, Bruhis M, Jain M, Embury J D, Mishra R K (2008) Constitutive behaviour of AA5754 sheet materials at large strains. Journal of Engineering Materials and Technology, 130:1-5.

Kelley E, Hosford W (1968) Plane-strain compression of magnesium and magnesium alloy crystals, Transactions of the Metallurgical Society of AIME, 242(1):5-13.

Klepaczko J R (1994) An experimental-technique for shear testing at high and very high strain rates-the case of a very mild steel. International Journal of Impact Engineering, 15:25-39.

Klepaczko J R, Nguyen H V, Nowacki W K (1999) Quasi-static and dynamic shearing of sheet metals. European Journal of Mechanics A/Solids, 18:271-289.

Kurukuri S, Worswick M J, Bardelcik A, Mishra R K, Carter J T (2014a) Constitutive behavior of commercial grade ZEK100 magnesium alloy sheet over a wide range of strain rates. Metallurgical and Materials Transactions A, 45:3321-3337.

Kurukuri S, Worswick M J, Ghaffari Tari D, Mishra R K, Carter J T (2014b) Rare-sensitivity and tension-compression asymmetry in AZ31B magnesium alloy sheet, Philosophical Transactions of the Royal Society A, 372:20130216.

Lademo O G, Engler O, Keller S, Berstad T, Pedersen K O, Hopperstad O S (2009) Identification and validation of constitutive model and fracture criterion for AlMgSi alloy with application to sheet forming, Materials and Design, 30:3005-3019.

Lian J, Sharaf M, Archie F, Munstermann S (2012) A hybrid approach for modelling of plasticity abd failure behaviour of advanced high-strength steel sheets, International Journal of Damage Mechanics, 22(2):188-218.

Lopes A B, Barlat F, Gracio J J, Ferreira Duarte J F, Rauch E F (2003) Effect of texture and microstructure on strain hardening anisotropy for aluminum deformed in uniaxial tension and simple shear, International Journal of Plasticity, 19:1-22.

Lou X Y, Li M, Boger R K, Agnew S R, Wagoner R H (2007) Hardening evolution of AZ31B Mg sheet, International Journal of Plasticity, 23:44-86.

Min J, Hector Jr L G, Lin J, Carter J T, Sachdev A K (2014) Spatio-temporal characteristics of propagative plastic instabilities in a rare earth containing magnesium alloy, International Journal of Plasticity, 57:52-76.

Mohr D, Henn S (2007) Calibration of stress-triaxiality dependant crack formation criteria: a new hybrid experimental-numerical method. Experimental Mechanics, 47:805-820.

Montheillet F, Cohen M, Jonas J J (1984) Axial stresses and texture development during the torsion testing of Al, Cu and α-Fe. Acta Metallurgica, 32(11):2077-2089.

Nemcko M J, Wilkinson D S (2016) Impact of microstructure on void growth and linkage in pure magnesium, International Journal of Fracture, DOI: 10.1007/s10704-016-0111-0.

Onaka S (2010) Equivalent strain in simple shear deformation described by using the Hencky strain, Philosophical Magazine Letters, 90(9):633-639.

Peirs J, Verleysen P, Degrieck J (2012) Novel technique for static and dynamic shear testing of Ti6Al4V sheet. Experimental Mechanics, 52:729-741.

Peirs J, Verleysen P, Tirry W, Rabet L, Schryvers D, Degrieck J (2011a) Dynamic shear localization in Ti6Al4V. Procedia Engineering, 10:2342-2347.

Peirs J, Verleysen P, Van Paepegem W, Degrieck J (2011b) Determining the stress-strain behaviour at large strains from high strain rate tensile and shear experiments. International Journal of Impact Engineering, 38:406-415.

Plunkett B, Cazacu O, Barlat F (2008) Orthotropic yield criteria for description of the anisotropy in tension and compression of sheet metals, International Journal of Plasticity, 24:847-866.

Rahmaan T, Butcher C, Abedini A, Worswick M J (2015) Effect of strain rate on shear properties and fracture characteristics of DP600 and AA5182-O sheet metal alloys, DYMAT 2015.

Rauch E F (2009) Plastic behavior of metals at large strains: experimental studies involving simple shear. Journal of Engineering Materials and Technology, 131:1-8.

Reyes A, Eriksson M, Lademo O G, Hopperstad O S, Langseth M (2009) Assessment of yield and fracture criteria using shear and bending tests. Materials and Design, 30:596-608.

Roth C C, Mohr D (2015) Ductile fracture experiments with locally proportional loading histories, International Journal of Plasticity, DOI: 10.1016/j.ijplas.2015.08.004.

Rusinek A, Klepaczko J R (2001) Shear testing of a sheet steel at wide range of strain rates and a constitutive relation with strain-rate and temperature dependence of the flow stress. International Journal of Plasticity, 17:87-115.

Schmid E, Boas W (1968) Plasticity of crystals, with special reference to metals, London Chapman & Hall.

Shi F F, Merle R, Hou B, Liu J G, Li Y L, Zhao H (2014) A critical analysis of plane shear tests under quasi-static and impact loading, International Journal of Impact Engineering, 74:107-119.

Steglich D, Tian X, Bohlen J, Kuwabara T (2014) Mechanical testing of thin sheet magnesium alloys in biaxial tension and uniaxial compression, Experimental Mechanics, 54:1247-1258.

Stout M G, O'Rourke J A (1989) Experimental deformation textures of OFE copper and 70:30 brass from wire drawing, compression, and torsion. Metallurgical and Materials Transactions A, 20A:125-131.

Tarigopula V, Hopperstad O S, Langseth M, Clausen A H, Hild F, Lademo O G, Eriksson M (2008) A study of large plastic deformations in dual phase steel using digital image correlation and FE analysis. Experimental Mechanics, 48(2):181-196.

Thuillier S, Manach P Y (2009) Comparison of the work-hardening of metallic sheets using tensile and shear strain paths, International Journal of Plasticity, 25:733-751.

Till E, Hackl B (2013) Calibration of plasticity and failure models for AHSS sheets, Proceedings of the International Deep Drawing Research Conference IDDRG 2013.

Wu L, Jain A, Brown D W, Stocia G M, Agnew S R, Clausen B, Fielden D E, Liaw P K (2008), Twinning-detwinning behavior during strain-controlled low-cycle fatigue testing of a wrought magnesium alloy, ZK60A, Acta Materialia, 56:688-695.

Yin Q, Brosius A, Tekkaya A E (2011), Modified plane torsion tests for sheet metal characterization, Steel Research International, special edition: 10th International Conference on Technology of Plasticity, ICTP, 1:696-701.

Yin Q, Soyarslan C, Guner A, Brosius A, Tekkaya A E (2012) A cyclic twin bridge shear test for the identification of kinematic hardening parameters, International Journal of Mechanical Sciences, 59:31-43.

Yoshida K, Ishii A, Tadano Y (2014) Work hardening behavior of polycrystalline aluminum alloy under multiaxial stress paths. International Journal of Plasticity, 53:17-39.